



AN ABSTRACT OF THE THESIS OF

Elizabeth J. Harper for the degree of Master of Science in Chemical Engineering presented on  
October 15, 2012

Title: Optimization of Capillary Trapping for CO<sub>2</sub> Sequestration in Saline Aquifers

Abstract approved:

---

Dorthe Wildenschild

Geological carbon sequestration, as a method of atmospheric greenhouse gas reduction, is at the technological forefront of the climate change movement. During sequestration, carbon dioxide (CO<sub>2</sub>) gas effluent is captured from coal fired power plants and is injected into a storage saline aquifer or depleted oil reservoir. In an effort to fully understand and optimize CO<sub>2</sub> trapping efficiency, the capillary trapping mechanisms that immobilize subsurface CO<sub>2</sub> were analyzed at the pore-scale. Pairs of proxy fluids representing the range of in situ supercritical CO<sub>2</sub> and brine conditions were used during experimentation. The two fluids (identified as wetting and non-wetting) were imbibed and drained from a flow cell apparatus containing a sintered glass bead column. Experimental and fluid parameters, such as interfacial tension, fluid viscosities and flow rate, were altered to characterize their relative impact on capillary trapping. Computed x-ray microtomography (CMT) was used to identify immobilized CO<sub>2</sub> (non-wetting fluid) volumes after imbibition and drainage events. CMT analyzed data suggests that capillary behavior in glass bead systems do not follow the same trends as in consolidated natural material systems. An analysis of the disconnected phases in both the initial and final flood events

indicate that the final (residual) amount of trapped non-wetting phase has a strong linear dependence on the original amount of non-wetting phase (after primary imbibition), which corresponds to the amount of gas or oil present in the formation prior to CO<sub>2</sub> injection. More importantly, the residual trapped gas was also observed to increase with increasing non-wetting fluid phase viscosity. This suggests that CO<sub>2</sub> sequestration can be optimized in two ways: through characterization of the trapped fluid present in the formation prior to injection and through alterations to the viscosity of supercritical CO<sub>2</sub>.

©Copyright by Elizabeth J. Harper  
October 15, 2012  
All Rights Reserved

Optimization of Capillary Trapping of CO<sub>2</sub> Sequestration in Saline Aquifers

by  
Elizabeth J. Harper

A THESIS

Submitted to

Oregon State University

in partial fulfillment of  
the requirements for the  
degree of

Master of Science

Presented October 15, 2012  
Commencement June 2013

Master of Science thesis of Elizabeth J. Harper presented on October 15, 2012.

APPROVED:

---

Major Professor, representing Chemical Engineering

---

Head of the School of Chemical, Biological and Environmental Engineering

---

Dean of the Graduate School

I understand that my thesis will become part of the permanent collection of Oregon State University libraries. My signature below authorizes release of my thesis to any reader upon request.

---

Elizabeth J. Harper, Author

## ACKNOWLEDGEMENTS

*“Silent gratitude isn’t much use to anyone”*  
– G.B. Stern

First and foremost, I would like to convey the sincerest of thanks to my advisor, Dr. Dorthe Wildenschild. Her excitement towards science (often in the form of experimentation) was truly infectious. Throughout this process, her support, guidance and encouragement have been instrumental in my development as a student and a scientist.

I would like to express heartfelt gratitude towards my fellow lab mates, Kendra Brown, Anna Herring, and Gabriel Iltis. Our shared brainstorming sessions, advice (thanks Gabe), laughter and many coffee breaks assisted me in more ways possibly enumerate here. A special thank you must also be extended to our former lab mate Ryan Armstrong, for providing much data analysis assistance (in the form of Avizo™) and for always being willing to answer *just one more question*.

I would also like to thank Manfred Dittrich for providing mechanical and engineering support that proved essential in the evolution and success of my experiments. Along that same vein, many thanks to Dr. Brian Bay, who not only allowed me to selfishly monopolize his micro-CT scanner for extended periods of time, but who also graciously provided maintenance support whenever necessary.

Perhaps most importantly, I would like to thank my friends and family for their endless love and support. Thanks to Keely Heintz for being such a great listener and friend who constantly and consistently brought humor into my life. It also goes without saying that I would not be who or

where I am today without the love of two amazingly selfless parents, Jim and Katie Harper. Words do not do their sacrifices justice. Thank you, Mom and Dad.

Last, but most certainly not least, thanks to Dr. Jeff Kimbrel for being my cheerleader, consummate champion, solid foundation and loving partner, thank you for everything you have done for me on this and all the future endeavors to come.

## TABLE OF CONTENTS

	<u>Page</u>
Chapter 1: Introduction.....	1
Chapter 2: Background.....	4
2.1 Fluids in Porous Media .....	4
2.2 Capillary Pressure .....	5
2.3 Drainage and Imbibition Processes .....	6
2.4 Capillary Pressure Saturation Curves.....	8
2.5 Capillary, Viscous and Gravitational Forces.....	9
2.6 Computed X-ray Microtomography .....	11
Chapter 3: Literature Review.....	13
3.1 Trapping Mechanisms .....	13
3.2 Capillary Trapping Research.....	15
3.3 Initial vs. Residual Saturation Trapping Models.....	17
3.4 Capillary Trapping Representations.....	19
3.5 Capillary Number Explored: Viscosity, Interfacial Tension and Flow Rate.....	22
3.5.1 Interfacial Tension and Viscosity.....	22
3.5.2 Flow Rate .....	24
Chapter 4: Materials and Methods.....	25
4.1 Bead Column.....	25
4.2 Fluid Pairs .....	25
4.3 Experimental Set-Up .....	27
4.4 Experimental Procedure .....	29
4.5 Scanning.....	31
4.6 Image Processing.....	31
4.6.1 Reconstruction.....	31
4.6.2 Segmentation .....	32
4.6.3 Voxel Calculations .....	36
4.7 Effects of Primary Imbibition.....	37
4.7.1 Initial Correlations and Reprocessing .....	37

## TABLE OF CONTENTS (Continued)

	<u>Page</u>
4.7.2 Primary Imbibition Dependence Quantification .....	39
Chapter 5: Results and Discussion .....	41
5.1 Dependence of Residual Saturation on Initial and Original Saturation.....	41
5.1.1 Residual versus Initial Trapping.....	41
5.1.2 Residual versus Original Trapping.....	42
5.2 Residual Trapping Results.....	49
5.2.1 Summary of Capillary Number Effects.....	49
5.2.2 Impact of Flow Rate .....	52
5.2.3 Interfacial Tension Effect.....	56
5.2.4 Effect of Viscosity Changes .....	58
5.2.4.1 Wetting Fluid Viscosity.....	58
5.2.4.2 Non-wetting Fluid Viscosity .....	59
Chapter 6: Conclusions.....	67
Future Work.....	70
Bibliography .....	71

## LIST OF FIGURES

<u>Figure</u>	<u>Page</u>
Figure 1.1 Carbon capture and storage schematic (DOE and NETL, 2007). .....	2
Figure 2.1: A capillary throat is occupied by a non-wetting and a wetting fluid (Blunt and Scher, 1995). .....	5
Figure 2.2: The formation of a liquid on a solid surface and the contact angle that it forms when it is at equilibrium (Dullien, 1992). .....	6
Figure 2.3: Trapped non-wetting fluid in the pore space (Gladkikh et al., 2006). .....	8
Figure 2.4: A capillary pressure saturation curve typical of immiscible fluids in porous media. ....	9
Figure 2.5: An x-ray CMT cone-beam configuration with a 360 <sup>0</sup> rotating stage. ....	11
Figure 3.1: Four CO <sub>2</sub> capture and storage trapping mechanisms and their relative storage security. ....	13
Figure 3.2: Literature values of initial versus residual non-wetting saturations with unconsolidated data points circled in red (Pentland et al., 2008). ....	18
Figure 3.3: Capillary de-saturation curve showing the trend of inversely proportional trend of decreasing residual saturation with increasing capillary number, $N_c$ (Cense and Berg, 2009). 19	
Figure 3.4: An example of 2D micro-model experimental data plotted on the Lenormand “phase diagram” (Zhang et al., 2011). .....	21
Figure 3.5: Decreasing capillary pressure in a non-wetting fluid (white) filled pore (a)-(c) (Nguyen et al., 2006). .....	22
Figure 4.1: A stacked schematic of the bead column experimental set-up. ....	27
Figure 4.2: A schematic of the set-up used in all proxy fluid experiments. ....	28
Figure 4.3: The experimental set up inside the CMT scanner hutch. ....	29
Figure 4.4: A summary of the three experimental steps: primary imbibition, drainage, and secondary imbibition. ....	30
Figure 4.5: Sample histogram containing voxel intensity values and the frequency in which they occur in a dry and wet grayscale volume. ....	33
Figure 4.6: Glass bead column slices during segmentation a) dry slice after image filtration, b) wet slices after image filtration, c) dry binarized slice and d) wet binarized slice. ....	35
Figure 4.7: Segmented volumes after a) initial segmentation with falsely binarized sections (white streaks), b) final segmentation with reassigned pixel values and three distinct phases. 36	
Figure 4.8: The relationship between <i>residual</i> non-wetting saturation and <i>original</i> non-wetting saturation prior to processing corrections (left) and after processing corrections (right). .....	38

## LIST OF FIGURES (Continued)

<u>Figure</u>	<u>Page</u>
Figure 4.9: Avizo™ generated isosurfaces depicting residual saturation reprocessing steps...	39
Figure 5.1: Percent initial, $S_i$ , and residual, $S_R$ , non-wetting saturations from seven proxy fluid pairs. ....	42
Figure 5.2: The relationship between <i>residual</i> non-wetting saturations, $S_R$ and <i>original</i> non-wetting phase saturations, $S_O$ , for all proxy fluid pairs.....	43
Figure 5.3: Avizo™ isosurfaces depicting the percent original saturation dependence. ....	44
Figure 5.4: Percent original non-wetting saturation dependence versus original non-wetting phase saturation for seven proxy fluid pair experiments. ....	45
Figure 5.5: Brine-air (left) and oil (right) experimental original saturation dependences plotted against their respective percent <i>original</i> non-wetting phase saturations. ....	46
Figure 5.6: Surfactant (left) and all glycerol (right) experimental original saturation dependences plotted as a function of percent residual non-wetting phase saturations. ....	47
Figure 5.7: Capillary numbers based on the invading fluid ( <i>wetting-phase</i> ) properties for the seven proxy fluid pairs plotted against their resulting <i>residual</i> non-wetting phase saturation. ....	50
Figure 5.8: Capillary number based on properties of the displaced fluid ( <i>non-wetting-phase</i> ) for the seven proxy fluids plotted against their resulting <i>residual</i> non-wetting saturations. ....	51
Figure 5.9: Residual non-wetting phase trapping, $S_R$ , for seven proxy fluid pairs as a function of secondary imbibition flow rate. ....	53
Figure 5.10: Percent residual non-wetting saturations, $S_R$ , plotted against secondary imbibition flow rate including the two additional flow rates at 250 mL/hr and 500 mL/hr.....	54
Figure 5.11: Three Avizo™ isosurfaces representing trapped non-wetting fluid from brine-octane experiments conducted over a range of secondary imbibition flow rates of 2-20 mL/hr. ....	55
Figure 5.12: Interfacial tension variation for the seven proxy fluid pairs plotted against percent residual non-wetting phase saturation.....	56
Figure 5.13: Interfacial tension $S_R$ comparison for (a) flow rate of 2 mL/hr and (b) flow rate of 20 mL/hr, for T1A and BO experiments.....	57
Figure 5.14: Proxy fluid pair data plotted in terms of wetting fluid viscosities against percent residual non-wetting saturations. ....	59
Figure 5.15: Residual non-wetting phase saturations versus non-wetting phase viscosities for the seven proxy fluids.....	60
Figure 5.16: Trapped residual non-wetting phase after secondary imbibition at 2mL/hr for proxy fluid pairs BA, BO and BS.....	61

## LIST OF FIGURES (Continued)

<u>Figure</u>	<u>Page</u>
Figure 5.17: Experimental mobility ratios ( $\mu_w/\mu_{NW}$ ) for the seven proxy fluid pairs are plotted as a function of their respective residual non-wetting phase saturations. ....	63
Figure 5.18: Proxy fluid experimental capillary number and mobility ratios plotted as a Lenormand phase diagram. ....	64
Figure 5.19: A plot of the product between capillary number (Ca) and the capillary-to-gravity ratio (CGR) versus the CGR. ....	65

## LIST OF TABLES

<u>Table</u>	<u>Page</u>
Table 4.1: Bead Core Specifics .....	25
Table 4.2: Experimental Fluid Characteristics .....	25
Table 5.1 Primary Imbibition Dependences .....	47
Table 5.2 Experimental wetting and non-wetting fluid viscosities.....	62

## Chapter 1: Introduction

Carbon dioxide (CO<sub>2</sub>) is a greenhouse gas emitted into the atmosphere through burning of fossil fuels for energy. Combustion of fossil fuels accounts for approximately 75% of the atmosphere's total anthropogenic CO<sub>2</sub> emissions and is currently released into the atmosphere at a rate higher than it can be removed by natural sources (IPCC, 2005). When it is released, CO<sub>2</sub> accumulates in the atmosphere and forms a barrier that adsorbs energy and prevents transfer of heat from Earth to space causing what is known as the Greenhouse Gas Effect. The Greenhouse Gas Effect causes a gradual warming of the earth and has led to numerous adverse climate effects such as surface and atmospheric temperature increase, sea level rise, loss of snow and ice cover and extreme weather events (IPCC, 2001).

Combustion of coal produces the most CO<sub>2</sub> per unit of energy compared to all other fossil fuels (Schrag, 2007) and remains a viable energy source as deep coal reserves in Russia, the United States, Australia, India and China are expected to last for the next 150 years (WEC, 2007). Given the projected time span and the current energy consumption rates, atmospheric emission reduction strategies must be developed to mitigate the negative impacts of CO<sub>2</sub> emissions. Of the viable options outlined by the Intergovernmental Panel on Climate Change (IPCC) the most mature mitigation strategy is CO<sub>2</sub> geologic storage, commonly referred to as carbon capture and storage (CCS).

CCS collects, concentrates and transfers a stream of CO<sub>2</sub> from combustion plants and injects it into the ground, as illustrated in Figure 1.1 (DOE and NETL, 2007). CO<sub>2</sub> is injected into formations at depths of approximately 800 meters. At this depth, CO<sub>2</sub> is present in its supercritical state; supercritical CO<sub>2</sub> is a very dense liquid that can behave like a gas. CO<sub>2</sub>

becomes supercritical at temperatures and pressures past its critical point of  $31^{\circ}\text{C}$  and  $7.4\text{ MPa}$  (Bandara et al., 2011).

Deep saline aquifers, in addition to depleted oil reservoirs where the injected supercritical  $\text{CO}_2$  can be used for enhanced oil recovery, are often sites of  $\text{CO}_2$  injection and storage due to their increased storage capacities, a single aquifer can store 1-10 gigatons (Benson et al., 2005), and high level of storage security.

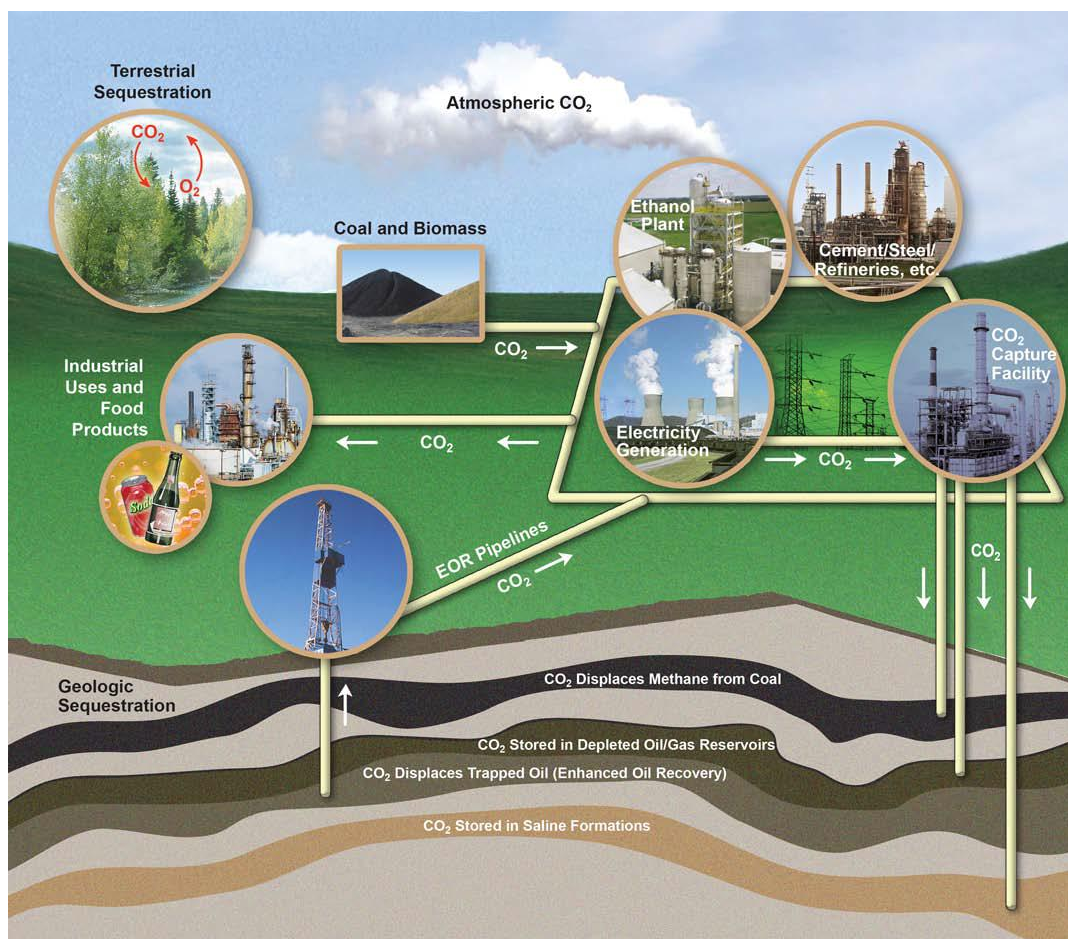


Figure 1.1 Carbon capture and storage schematic (DOE and NETL, 2007).

The success of a CCS project depends on its ability to efficiently trap CO<sub>2</sub> in the subsurface for hundreds and even thousands of years. In order to ensure security and prevent leakage, the physical and chemical mechanisms that trap CO<sub>2</sub> must be understood. While many academic and industrial institutions have investigated various trapping mechanisms, more exploration is needed to fully understand and optimize CO<sub>2</sub> trapping.

## Chapter 2: Background

### 2.1 Fluids in Porous Media

Porous media refers to areas of material that are devoid of solid. Porous media are of interest in environmental applications because of the fluids they transport and store in subsurface sands, soils and rocks. Examples of fluids transported through the pore space include groundwater flow through aquifers, oceanic salt water intruding on freshwater sources, hydrocarbon (oil) being extracted from deep sedimentary rocks, and CO<sub>2</sub> being sequestered in geological formations.

In this thesis, porous media is referred to as either consolidated or unconsolidated. Consolidated media, such as limestone or sandstone, are materials that have become compacted or cemented over time. Unconsolidated media, such as sand or gravel, are typically deposits that are not densely packed and have larger pore spaces for fluids to pass through.

When fluid pairs, such as water/oil or water/gas, that have limited mutual solubility form separate phases, they are called immiscible (or non-mixing) fluids. In an immiscible system, one fluid is considered wetting and the other non-wetting. This distinction is the result of one fluid having a stronger attraction to adsorb to the surrounding solid phase than the other. In a water-wet porous medium where two phases are present, such as water and gas, the solid will preferentially be surrounded by water because the attractive forces are stronger between the water and the soil than the gas and the soil. When two or more immiscible fluids occupy the same pore space they form a thin boundary layer called an interface where they meet (Figure 2.1).

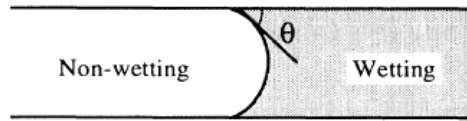


**Figure 2.1: A capillary throat is occupied by a non-wetting and a wetting fluid (Blunt and Scher, 1995).**

The distribution of the wetting and non-wetting fluids in a two-phase system is determined by the pore geometry and the wettability of the medium (wettability refers to the preferentially stronger attraction of the solid to either the wetting or non-wetting fluid). The wettability of a solid will dictate how fluids move throughout the pore space. A solid's wettability is typically classified as water-wet, intermediate-wet or oil-wet (Corey, 1994). Many reservoirs considered for geological sequestration of atmospheric gases (often saline aquifers) are considered water-wet. Whereas in enhanced oil recovery applications, the oil reservoirs are often assumed to be oil-wet because of the prolonged exposure to hydrocarbons.

## 2.2 Capillary Pressure

The interfacial interaction between two fluids is represented by capillary pressure. Capillary pressure ( $P_c$ ) is defined as the difference between the non-wetting fluid pressure ( $P_{nw}$ ) and the wetting fluid pressure ( $P_w$ ) and is a function of the wetting phase saturation ( $S_w$ ):

$$P_c(S_w) = P_{NW} - P_W \quad (\text{eq. 2.1})$$

This relationship between capillary pressure, interfacial tension, wettability and pore size is described by the Young-Laplace equation which is widely used to calculate the capillary pressure in a tube of radius,  $R$ .

$$P_c = \frac{2\sigma \cos \theta}{R} \quad (\text{eq. 2.2})$$

where  $\sigma$  represents the interfacial or surface tension between the two static fluids and  $\Theta$  is the contact angle, i.e. the angle that forms at the solid surface. Two-phase fluid systems with  $\Theta$  approximately equal to  $0^\circ$  are water-wet,  $\Theta$  between  $0^\circ$  and  $90^\circ$  are intermediate-wet and systems with  $\Theta$  approximately equal to  $180^\circ$  are oil-wet. Wettability is determined by a force balance between adhesive and cohesive forces. A contact angle that is formed in a theoretical two-phase system is shown in Figure 2.2.

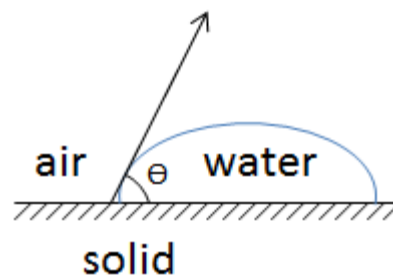


**Figure 2.2: The formation of a liquid on a solid surface and the contact angle that it forms when it is at equilibrium (Dullien, 1992).**

In water wet systems, with a contact angle of zero, Equation 2.2 simplifies to Equation 2.3 and shows that capillary pressure is inversely proportional to the pore radius.

$$P_c = \frac{2\sigma}{R} \quad (\text{eq. 2.3})$$

### 2.3 Drainage and Imbibition Processes

Flow events through porous media are often defined as imbibition and drainage processes. In a two fluid phase system, imbibition refers to the wetting fluid invading the pore space and displacing the non-wetting fluid. Drainage refers to the non-wetting fluid invading the pore space and displacing the wetting fluid.

In this work, three flow events take place: primary imbibition, primary drainage and secondary imbibition of a porous medium. Primary imbibition is defined as the process in which the porous medium is initially saturated with wetting fluid. When primary imbibition is complete the water in the pores are at a hydrostatic pressure of zero. The purpose of primary imbibition is to achieve a condition that represents a saturated aquifer that is found at a CO<sub>2</sub> sequestration site.

Once primary imbibition is completed, the sample is drained of wetting fluid during the primary drainage event; this is equivalent to the CO<sub>2</sub> injection phase. Not all of the wetting fluid will drain as an irreducible amount of wetting fluid saturation, denoted as  $S_{irr}$ , will remain trapped in the pore space. The  $S_{irr}$  is typically located in the media's smallest pores because the capillary forces required to remove the fluid from those pores is too large to overcome, as shown by the simplified Laplace's Law in Equation 2.3. According to this law, wetting fluid leaves the larger radii pores first because they have the lowest capillary pressure threshold. Correspondingly, small pores retaining the wetting fluid are surrounded by empty larger pores and they become isolated from the rest of the wetting phase. Even though the capillary pressure will continue to increase, the now disconnected fluid in the small pores will not be able to leave the pore space. The capillary pressure will continue to increase until drainage is forcibly stopped (in physical injection scenarios) or until the system equilibrates naturally.

The reverse process occurs during a subsequent imbibition event. Wetting fluid is re-imbibed into the pore space and preferentially fills the smaller pores first because of the reduced capillary pressure requirements. Due to the pressure differences between the wetting and non-wetting fluids, the non-wetting fluid may become surrounded by wetting fluid during this

process, as seen in Figure 2.3. As was also observed in drainage events, once a fluid is disconnected from the rest of its fluid phase, it will not be able to leave the pore space, except in the very slow process of fluid film flow. It is during this secondary imbibition event that CO<sub>2</sub> is trapped in CCS. This happens when displaced formation water (brine) re-enters the injection zone, or during engineered water (or brine) floods.

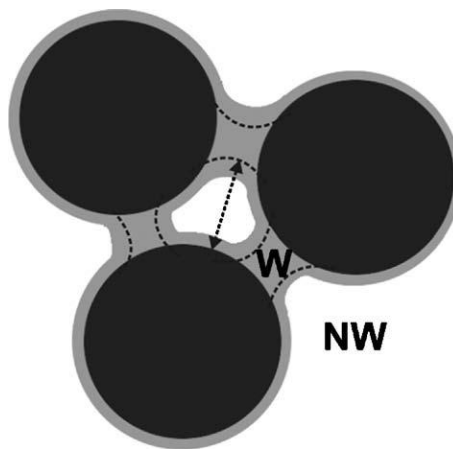


**Figure 2.3: Trapped non-wetting fluid in the pore space (Gladkikh et al., 2006).**

## 2.4 Capillary Pressure Saturation Curves

Capillary pressure changes with saturation during drainage and imbibition events. The relationship follows a distinct s-shaped curve and is depicted in Figure 2.4 in what is known as a  $P_c$ -S curve.  $P_c$ -S curves are unique to different types of porous media and they provide valuable insight into formation characteristics such as storage capacity, porosity and relative permeability.

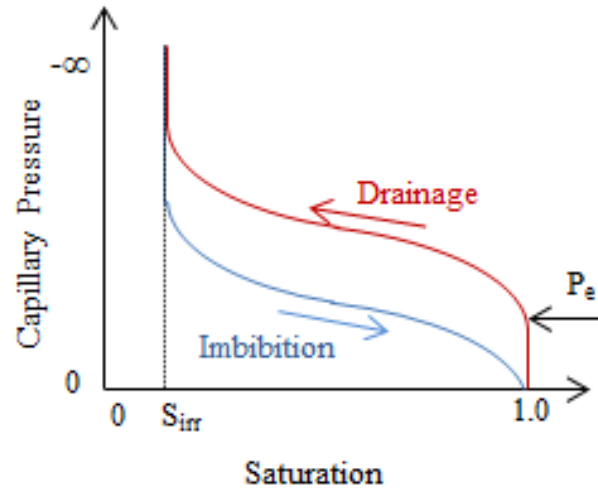


**Figure 2.4: A capillary pressure saturation curve typical of immiscible fluids in porous media.**

When a porous medium is fully saturated ( $S = 1.0$ ), the pressure required for the non-wetting phase to invade the medium in a drainage event is called the “entry” pressure ( $P_e$ ). Since capillary pressure is inversely proportional to pore radius, the non-wetting phase will only enter the pore space when the capillary pressure ( $P_e$ ) associated with the pore with the smallest radius has been exceeded. The magnitude of  $P_e$  will vary depending on the medium, fluid properties and pore size distribution.

## 2.5 Capillary, Viscous and Gravitational Forces

In two-phase immiscible fluid systems, capillary number,  $Ca$ , is a dimensionless number that is used to describe the ratio between capillary forces and viscous forces and is the variable that has been shown to be a predictor of trapping efficiency for non-wetting phase trapping in porous media. There are many different definitions of capillary number, some of which incorporate relative permeability, however for the purposes of this research,  $Ca$  is defined as:

$$Ca = \frac{\text{viscous forces}}{\text{capillary forces}} = \frac{\mu v}{\sigma} \quad (\text{eq. 2.4})$$

where  $\mu$  is the viscosity of the invading fluid,  $v$  is the pore velocity of the invading fluid and  $\sigma$  is the interfacial tension between the invading and displacing fluids (Morrow et al., 1988; Suekane et al., 2008; Heiss et al., 2011). The role of the invading or displacing fluid changes between imbibition and drainage events.

The mobility ratio,  $M$ , is often used as a method of comparing the relative effect of the viscosities of the non-wetting and wetting fluid phases in trapping of fluids in porous media. Like the capillary number, there are multiple definitions for mobility ratio. The mobility ratio chosen for this research is:

$$M = \frac{\mu_i}{\mu_d} \quad (\text{eq. 2.5})$$

where  $\mu_i$  represents the viscosity of the invading fluid and  $\mu_d$  represents the viscosity of the displacing fluid (Lenormand et al., 1988; Zhang et al., 2011).

Similarly, the capillary-to-gravity ratio (CGR) provides a means of quantifying the relative impact of gravity on the system. The CGR is often plotted in conjunction with the capillary number to identify which of the three forces: capillary, viscous, or gravitational, dominate at the pore-scale during fluid displacement. CGR is defined as:

$$CGR = \frac{2\sigma}{\Delta\rho * g * h * \sqrt{\frac{k}{\Phi}}} \quad (\text{eq. 2.6})$$

where  $\sigma$  is the interfacial tension between the invading and displacing fluids,  $\Delta\rho$  is the difference in density between the invading and displacing fluids,  $g$  is the gravitational constant,  $h$  is height of the system,  $k$  is the theoretical permeability and  $\Phi$  is the porosity of the system.

The permeability can be calculated as:

$$k = \frac{\phi^{5.5}}{5.6} d^2 \quad (\text{eq. 2.7})$$

where  $d$  is the diameter of the glass beads (Polak et al., 2011).

## 2.6 Computed X-ray Microtomography

Computed x-ray microtomography (CMT) is a non-invasive method of imaging the structure of an unknown material or sample and is used in a vast number of applications, across a number of scientific disciplines. CMT was utilized in this work to collect images of fluid distributions within a porous medium after imbibition and drainage events.

There are many different types of CMT configurations, an example of the configuration used for data collection in this research is shown in Figure 2.5.

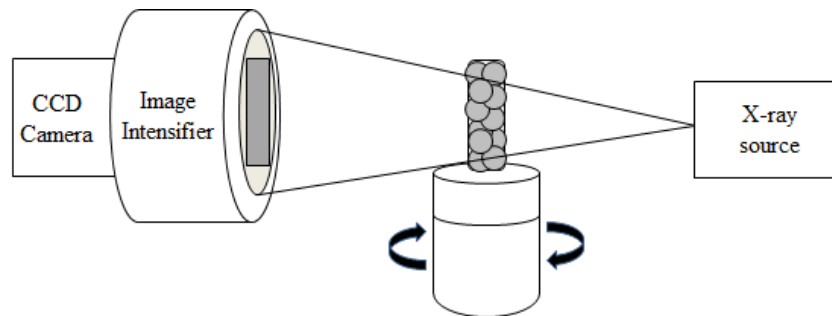


**Figure 2.5: An x-ray CMT cone-beam configuration with a 360° rotating stage.**

The x-ray source transmits x-rays in cone formation through a selected sample positioned on a rotating stage. Different sample materials have the ability to scatter and adsorb x-rays. Since certain phases attenuate x-rays similarly, dopants with known attenuation coefficients can be added to a fluid phase to increase contrast during image analysis.

For a monochromatic radiation source, the attenuated intensity (or reduced intensity) of the x-ray beam that is transmitted through the sample is represented by Lambert-Beer's Law:

$$I = I_o \exp(-\mu D) \quad (\text{eq. 2.8})$$

Where  $I_o$  is the beam's incident intensity,  $\mu$  is the linear attenuation coefficient of the sample and  $D$  is the sample thickness.

The intensity information transmitted through the sample is detected by an x-ray sensitive detector, converted to visible light and generally imaged by a charge coupled device (CCD) camera as two dimensional radiographs (Wildenschild et al., 2002). The radiographs are collected over range of angles which are then reconstructed using a computationally intensive algorithm into a three dimensional (3D) grayscale image.

The spatial resolution of a computed tomography (CT) system describes the level to which sample detail can be resolved in the reconstructed images, and varies depending on the application. In medical devices, the resolution generally ranges from 200-500 micrometers ( $\mu\text{m}$ ) per pixel, while laboratory or industrial CMT systems can achieve resolutions down to 5-10  $\mu\text{m}$  (Wildenschild et al., 2002). The CMT system that was utilized for the work presented here has a focal spot size of 3.75  $\mu\text{m}$ , which is the maximum attainable resolution. For the sample size used (5.7 millimeters in diameter) the resulting resolution was approximately 13 micrometers per pixel. In general, sharper or higher quality images are obtained as the spatial resolution improves.

## Chapter 3: Literature Review

### 3.1 Trapping Mechanisms

CO<sub>2</sub> is immobilized in the subsurface by the four following mechanisms: (1) structural trapping, (2) dissolution trapping, (3) mineral trapping and (4) capillary trapping. Figure 3.1 is a representation of all four mechanisms in relation to the time required to induce trapping as well as the storage security of each method (IPCC, 2005).

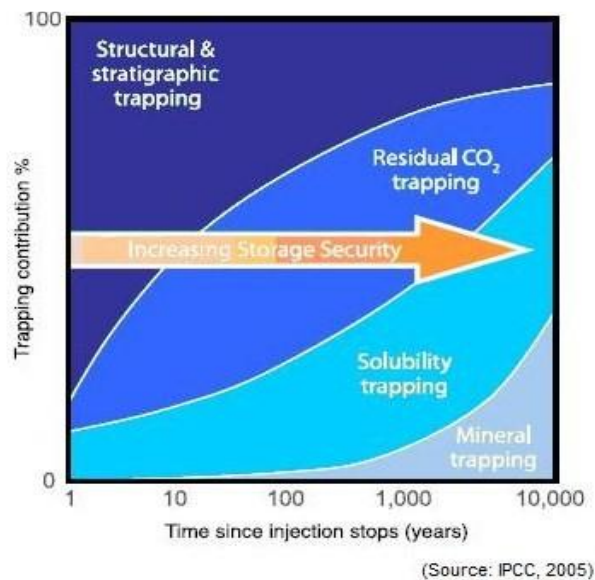


**Figure 3.1: Four CO<sub>2</sub> capture and storage trapping mechanisms and their relative storage security.**

Structural or hydrodynamic trapping occurs when CO<sub>2</sub> is immobilized by the geology of the storage area. When CO<sub>2</sub> is injected into an aquifer it has the tendency to migrate upwards due to the density difference between the CO<sub>2</sub> and the in-situ brine. Storage sites that have an impermeable cap rock covering the storage zone are specifically selected to prevent CO<sub>2</sub> migration. A study done on formations in the Alberta Basin determined that an injection

formation must be sealed with an impermeable layer or an aquitard to induce hydrodynamic trapping (Bachu et al., 1994).

Despite its simplicity, structural trapping is the least secure of the storage mechanisms. Improperly trapped CO<sub>2</sub> can leak out of an aquifer through cracks or abandoned injection wells left by oil and gas explorations (Nordbotten et al., 2004). To prevent these leaks, specifically those caused by pressure fissures, cap rocks must be of sufficient width (at least 100 meters) to effectively trap CO<sub>2</sub> in the subsurface (Rutqvist and Tsang, 2002).

The second mechanism is dissolution trapping, which occurs when injected CO<sub>2</sub> dissolves in the surrounding in-situ brine. Dissolution trapping is enhanced by convective mixing as less-dense CO<sub>2</sub> migrates upwards through the in-situ brine (Ennis-King and Paterson, 2005; Riaz et al., 2006). In an effort to optimize these dissolution mechanisms, Qi (2009) proposed an improved capture strategy of injecting CO<sub>2</sub> and brine together followed by an injection of chase brine. Varied compositions of the mixed stream yielded 80-95% trapping efficiency of CO<sub>2</sub>.

Mineral trapping may take place subsequent to dissolution trapping if CO<sub>2</sub> reacts with minerals in geologic formations to form carbonate precipitates. While mineral trapping occurs over longer time spans than other mechanisms (on the order of thousands of years), it is more effective for immobilizing CO<sub>2</sub> than dissolution trapping (Gunter et al., 1997). Yet, the precipitate that forms during dissolution trapping can reduce overall porosity and thereby limit the injection capacity of the formation (Xu et al., 2004). Despite the benefits of increased storage security, mineral trapping is often not a feasible trapping solution, particularly in

instances when the capacity of the formation decreases with time due to precipitate build up, but also because of the long time scales involved.

The final mechanism, and the focus of this work, is capillary or residual trapping. Capillary trapping is arguably the most advantageous form of trapping because of its high storage security and relatively short time requirements (Juanes et al., 2006). The capillary trapping mechanism can also have a greater effect on overall trapping than dissolution or mineral trapping mechanisms in CO<sub>2</sub> sequestration (Kumar et al., 2004). Capillary trapping has been the focus of many investigations because the ultimate volume of CO<sub>2</sub> trapped in the subsurface has been shown to be highly dependent on capillary forces. Potentially all of the injected CO<sub>2</sub>, under specific formation and time conditions, can be trapped by capillary forces (Benson et al., 2005).

### **3.2 Capillary Trapping Research**

Many researchers have examined the effect of capillary trapping, with varying methodologies and results, for application in both CO<sub>2</sub> sequestration and enhanced oil recovery. Some of the techniques, parameters of interest, and contrasting results presented in recently published capillary trapping research are summarized below.

CMT imaging and modeling software have produced capillary pressure-saturation curves and fluid distribution information that has effectively matched experimental data in consolidated media; thus proving the predictive capability of these two capillary trapping quantification techniques (Silin et al., 2011). CMT imaging has also been used to measure the storage security of residual trapped non-wetting phase (CO<sub>2</sub>). Residual saturations of supercritical CO<sub>2</sub> in quartz sandstone were measured at 25% and local capillary trapping was determined a safe and

effective method of securing supercritical CO<sub>2</sub> in the subsurface by Iglauer et al., (2011). Pentland et al., (2011) measured somewhat higher trapping capacities with maximum residual non-wetting phase saturations of 35% and 48% in brine-supercritical CO<sub>2</sub> and brine-oil experiments, respectively.

Capillary heterogeneity can also have an effect on non-wetting phase saturation distribution. CMT images of capillary trapping experiments on homogeneous and heterogeneous sandstone samples showed that the heterogeneous sample had widely varying wetting and non-wetting saturations and irregular capillary-pressure saturation curves (Pini et al., 2012). Additionally, research has shown that poorly consolidated media produces low residual non-wetting phase saturations (4-6%), thus indicating that well consolidated media would be better suited for CO<sub>2</sub> injection scenarios (Al Mansoori et al., 2009).

The impact of capillary forces (presented in terms of fluid flow rate, viscosity, and interfacial tension) on initial and residual trapping have been initially investigated by Wildenschild et al., (2010). Proxy fluid pair experiments on glass bead packs suggested that *initial* non-wetting phase saturations were optimized at low drainage (i.e. non-wetting fluid) flow rates and decreasing non-wetting phase viscosities. *Residual* non-wetting phase saturations were optimized at high imbibition (i.e. wetting fluid) flow rates and increasing non-wetting phase viscosities; however, the authors determined that further experimentation was required to substantiate these results.

The effects of gravitational forces on capillary trapping were investigated by Bandara et al., (2011). When gravity forces are small, CO<sub>2</sub> can be effectively trapped by capillary forces. When

gravity forces are large, CO<sub>2</sub> can be more mobile and overall trapping efficiency may decrease. Suekane et al., (2010) also found that gravitational effects can influence residual trapped non-wetting phase, but in their glass bead experiments the gravitational forces were approximately 23 times higher than might naturally occur in a CO<sub>2</sub> injection reservoir.

In residual oil recovery research, media wettability and non-wetting fluid saturation history (i.e. initial saturation) has been shown to play a role in capillary trapping of non-wetting fluid in the pore space. The non-wetting phase (oil) distribution within the pore space can change with wettability in water-wet and mixed water-wet systems. The volume of residual non-wetting phase saturation was shown to be dependent on initial non-wetting phase saturation (Kumar et al., 2009). This relationship between initial and residual non-wetting phase saturation has been widely researched and is described in greater detail in the following section.

### **3.3 Initial vs. Residual Saturation Trapping Models**

Capillary trapping efficiency is a measurement of the amount of residual trapped gas (or non-wetting phase) in the subsurface. The dependence of residual trapped gas (after imbibition events) on initial trapped gas (after drainage events) has been extensively studied in porous media research (Pentland et al., 2008; Pentland et al., 2010). Resulting initial and residual saturation trends are often described by the traditional Land's model, which is shown in Figure 3.2 (Pentland et al., 2008). The unconsolidated data points, denoted by red circles, follow the Land's model.

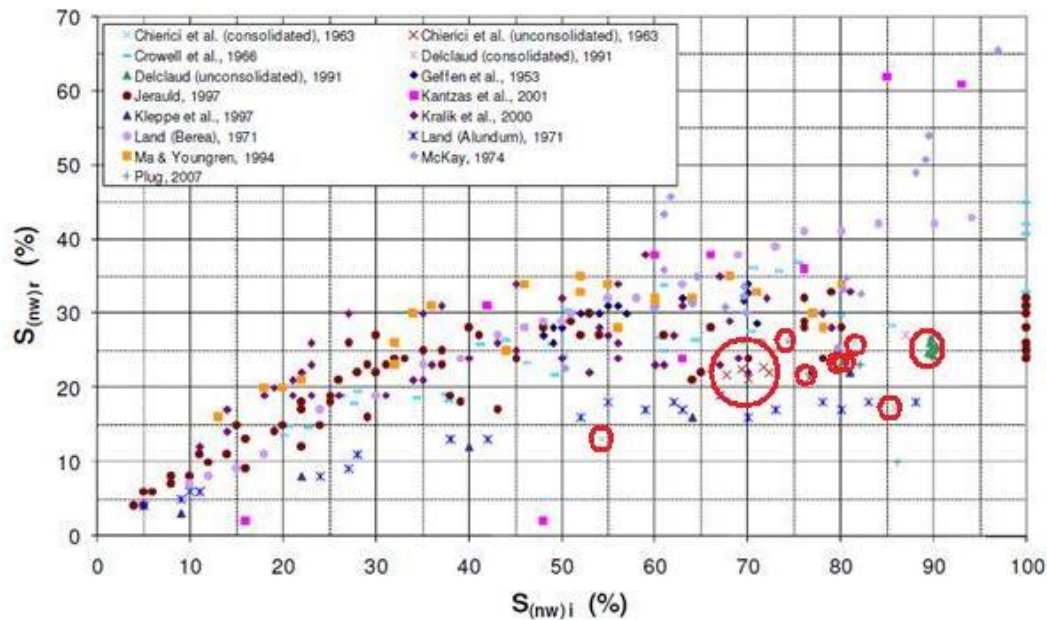


**Figure 3.2: Literature values of initial versus residual non-wetting saturations with unconsolidated data points circled in red (Pentland et al., 2008).**

Land (1968) originally developed an empirical relationship between initial and residual non-wetting saturations for two-phase flow in water-wet consolidated media:

$$S_{gr}^* = \frac{S_{gi}^*}{1 + CS_{gi}^*} \quad (\text{eq. 3.1})$$

where  $S_{gr}^*$  is the residual gas (non-wetting) saturation,  $S_{gi}^*$  is the initial gas (non-wetting) saturation and  $C$ , Land's coefficient, is based on the maximum residual gas saturation,  $S_{gr}^{*max}$  the maximum residual non-wetting saturation.  $C$  is defined as:

$$C = \frac{1}{S_{gr}^{*max}} - 1 \quad (\text{eq. 3.2})$$

Not all initial versus residual trapping experiments match the above Land's model; data sets can instead be matched to other empirical trapping models (e. g. Aissaoui, 1983; Spiteri et al., 2008). Whichever model is selected, these relationships are useful for predicting the

characteristics of relative permeability hysteresis based on the calculated residual non-wetting ( $\text{CO}_2$ ) saturation (Kumar et al., 2004; Juanes et al., 2006).

### 3.4 Capillary Trapping Representations

The residual non-wetting phase saturation is dependent on the capillary number (Lenormand et al., 1983; Lenormand et al., 1988; Morrow et al., 1988; Blunt and Scher, 1995; Zhang et al., 2011). Capillary number, as mentioned previously, is the ratio between fluid flow rate and viscosity, and interfacial tension. This dependence of residual saturation on capillary number is often illustrated by the capillary de-saturation curve. This curve, shown in Figure 3.3 (Cense and Berg, 2009), indicates that residual saturation decreases with increasing capillary number (Chatzis and Morrow, 1984) and shows the critical capillary number (the capillary number,  $N_c$ , at which the residual saturation begins to decline) at approximately  $10^{-5}$  and  $10^{-3}$  for non-wetting and wetting phase trapping, respectively.

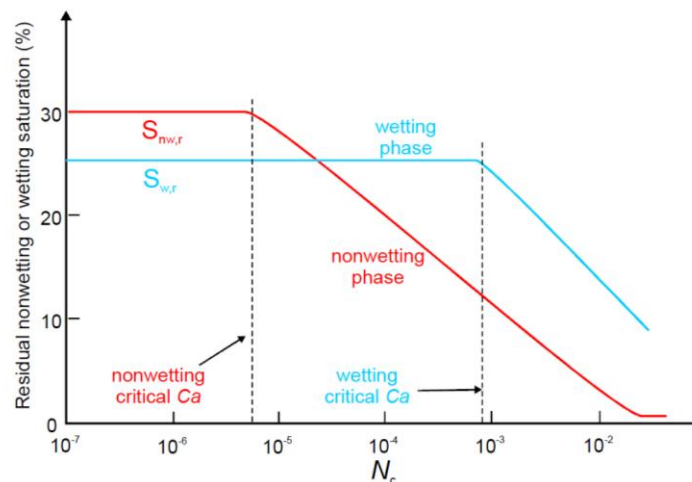


**Figure 3.3: Capillary de-saturation curve showing the trend of inversely proportional trend of decreasing residual saturation with increasing capillary number,  $N_c$  (Cense and Berg, 2009).**

This trend has been shown to hold for many different types of porous media. Ding and Kantzas (2007) conducted two-phase experiments on Berea sandstone and determined critical non-wetting phase capillary numbers of  $10^{-5}$  for water-oil systems and  $10^{-8}$  for water-gas systems. Shen et al., (2010) explored non-wetting critical capillary numbers in Chinese sandstones of intermediate permeability; the capillary number was several orders of magnitude higher at  $10^{-3}$ , suggesting that porous media characteristics have a strong influence on capillary trapping behavior. This conclusion was confirmed by critical capillary numbers observed in glass bead packs, which were approximately two orders of magnitude ( $10^{-4}$ ) higher than consolidated sandstone materials (Chatzis et al., 1988).

Capillary numbers are often plotted against mobility ratios as a method of visualizing the dependence of viscous forces to capillary forces. Based on the resulting plot, three distinct regimes emerge and are defined as viscous fingering, capillary fingering, and stable displacement regimes (Lenormand et al., 1988). Figure 3.4 is an example of such a Lenormand “phase diagram”. The experimental data from Zhang et al., (2011) confirmed previous findings that non-wetting residual saturations were higher in regions of capillary fingering in fluid flow through 2D micro-models. In capillary fingering, the invading wetting fluid flow is controlled by capillary forces in the pore space, which leads to an unstable, branch-like fluid displacement front.

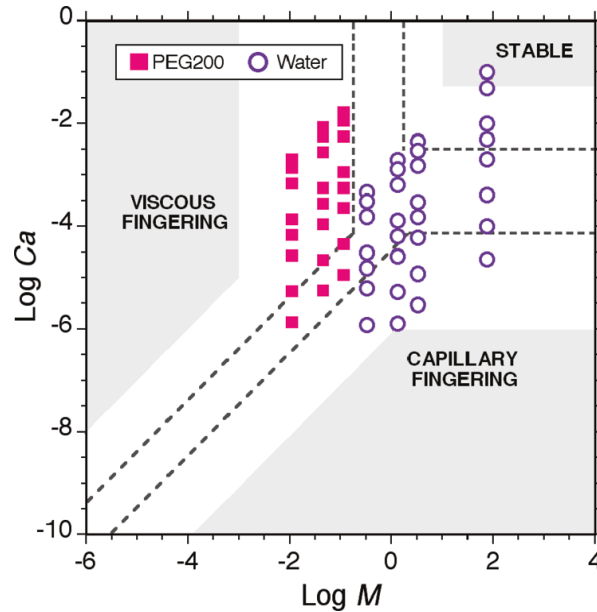


**Figure 3.4:** An example of 2D micro-model experimental data plotted on the Lenormand “phase diagram” (Zhang et al., 2011).

The physical mechanisms in which immiscible fluids are displaced inside the pore include events such as piston-like displacement, snap off, and cooperative pore body filling. The mechanism of snap-off is important for trapping of non-wetting phase and occurs in the capillary fingering regime (Lenormand et al., 1983). Snap-off immobilizes gas in the trailing end of the migrating CO<sub>2</sub> plume and is the dominant displacement mechanism in capillary trapping (Valvatne and Blunt, 2004). Figure 3.5 shows how the process of snap-off occurs in the pore space with decreasing capillary pressure: corner wetting films grow and eventually coalesce and trap the non-wetting phase. Snap off is favored by slow displacement rates, high pore-throat aspect ratios, and zero contact angles (Nguyen et al., 2006).

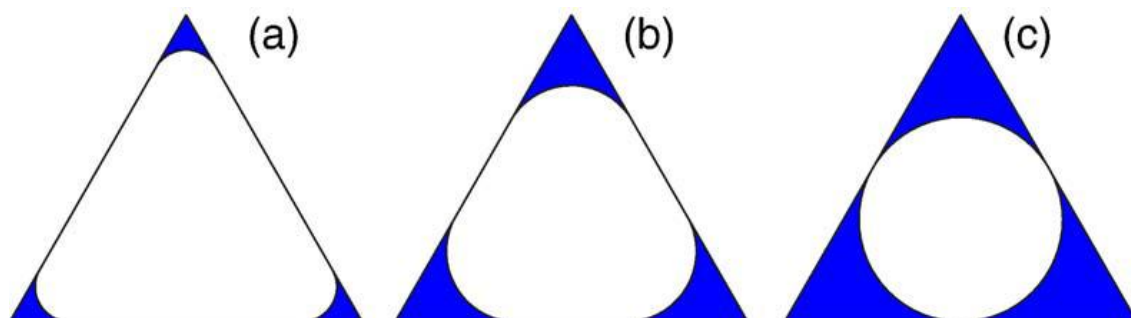


**Figure 3.5: Decreasing capillary pressure in a non-wetting fluid (white) filled pore (a)-(c) (Nguyen et al., 2006).**

Based on the Lenormand phase diagram, it is possible to optimize capillary numbers and mobility ratios to move a system from the viscous fingering and stable displacement regimes to the capillary fingering regime, thus inducing snap-off and increasing residual trapping.

### 3.5 Capillary Number Explored: Viscosity, Interfacial Tension and Flow Rate

The aim of CO<sub>2</sub> sequestration is to maximize the amount of trapped CO<sub>2</sub> in the subsurface and to prevent it from migrating upwards. The capillary de-saturation curve and the Lenormand phase diagram present a means of obtaining this goal through alterations made to the capillary number. Recent research has explored the relative effect of the three *individual* elements of capillary number (interfacial tension, viscosity and flow rate) on residual trapping and their findings are summarized in the following sections.

#### 3.5.1 Interfacial Tension and Viscosity

Increasing viscosity and interfacial tension values were shown to increase residual CO<sub>2</sub> saturations in consolidated sandstone samples collected from a site in Alberta, Canada (Bennion and Bachu, 2005; Bennion, 2006a; Bennion and Bachu, 2006b; Bennion and Bachu, 2006c).

Further investigation confirmed the trend of increasing trapped CO<sub>2</sub> saturation during imbibition events with increasing interfacial tension (Bachu and Bennion, 2008). Trapped CO<sub>2</sub> was also observed to increase with increasing mobility ratio (with brine as the invading fluid and supercritical CO<sub>2</sub> as the displacing fluid) which was varied by changing pressure and temperature conditions. Since the interfacial tension and viscosity values were both dependent on pressure, temperature, and salinity in this research, it was not possible to isolate the viscosity trends and instead the authors concluded that the increasing residual CO<sub>2</sub> trapping with viscosity ratio was related to increasing interfacial tension trend. The authors stated that it would be impossible to design a supercritical CO<sub>2</sub> experiment that isolates interfacial tension effects from viscous effects; however that should not prevent us from understanding which fluid property is most important on overall trapping.

Altered interfacial tension and viscosity values were studied in experiments on unconsolidated and sintered bead packs with capillary numbers ranging from  $10^{-3}$  to  $10^{-4}$  (Morrow et al., 1988). In the enhanced oil recovery research, capillary numbers for oil mobilization were approximately an order of magnitude higher in bead packs than consolidated sandstones; but the glass beads still followed a trend of increasing residual non-wetting phase saturation with a decreasing capillary number. The changing interfacial tension between the non-wetting and wetting phase did not have an effect on the residual trapping trend. The effects of the changing viscosities were not isolated and conclusions regarding its relative effect on trapping efficiency could not be determined.

### 3.5.2 Flow Rate

A consensus regarding the effects of flow rate on capillary number and residual trapping has yet to be reached. Blunt and Scher (1995) investigated the effects of flow rate on immiscible fluid displacement in a pore-network model for application in oil reservoirs. The authors determined that the dominant fluid displacement mechanism will change depending on flow rate due to fluid competition at the pore-scale. Nguyen et al. (2006) produced high residual non-wetting saturations through a study of the snap-off mechanism, which was favored at low flow rates, high aspect ratios and small contact angles. Most research supports this finding, arguing that snap off is suppressed at high flow rates; however, Juanes et al. (2006) simulated that snap off will increase residual trapping at faster injection rates of supercritical CO<sub>2</sub> due to increased capillary pressure in small pores. Wildenschild et al., (2011) showed a weak relationship between increased residual non-wetting phase and increasing flow rate.

To our knowledge no work has been published that examines *both* the isolated and combined impacts of the three elements of capillary number as a means of optimizing CO<sub>2</sub> trapping efficiency. Further investigation is needed to bring clarity to issues related to capillary number and its effect on residual trapping.

## Chapter 4: Materials and Methods

### 4.1 Bead Column

All experiments were performed on two sintered, soda lime glass bead columns. The columns were a mixture consisting of 35% 600  $\mu\text{m}$ , 35% 850  $\mu\text{m}$  and 30% 1-1.4 mm size beads. The beads were sintered to a borosilicate glass pipette column using a graphite crucible in a muffle oven at 760<sup>o</sup> Celsius. The two column specifications and their respective sintered porosities are summarized below in Table 4.1.

Table 4.1: Bead Core Specifics			
Core	Height (mm)	Diameter (mm)	Measured Porosity
1	57.31	5.67	33.4%
2	56.33	5.71	34.7%

### 4.2 Fluid Pairs

Experiments were conducted using seven pairs of proxy fluids, chosen to largely represent the range of interfacial tensions, viscosities, and flow rates exhibited by supercritical CO<sub>2</sub> during CCS injection. The injection parameters of proxy fluids and supercritical CO<sub>2</sub> are described in Table 4.2.

Table 4.2: Experimental Fluid Characteristics	
	Supercritical CO <sub>2</sub> , Approximate Range (Lenormand et al., 1983)
Interfacial tension (dynes/cm)	25-50
Viscosity (cP)	0.025 – 0.15

Density (g/cm <sup>3</sup> )	465-900			
	<b>Non-Wetting Fluids (paired with wetting fluid: brine)</b>			
	air	octane	Soltrol 220	
Interfacial tension (dynes/cm)	72	37	25	
Viscosity (cP)	0.018	0.54	4.82	
Density (g/cm <sup>3</sup> )	0.001	0.710	0.790	
	<b>Wetting Fluids (paired with non-wetting fluid: air)</b>			
	Triton 1	Triton 2	glycerol 1	glycerol 2
Interfacial tension (dynes/cm)	37	50.9	66	69
Viscosity (cP)	1.13	1.13	1.86	3.95
Density (g/cm <sup>3</sup> )	1.08	1.08	1.145	1.207

The wetting fluids were all potassium iodide (KI) brine based. Solutions consisted of a 1:6 mass ratio of KI to deionized water. The solution ratio was designed to attenuate the x-rays that were transmitted through the wetting phase, thus increasing the contrast of the wetting phase in the 2D radiographic images. The contrast between the phases provided an easier means of segmenting the images during data analysis.

The four additional wetting phase fluids consisted of KI brine and varying concentrations of Triton 100X surfactant and glycerol. Triton 100X was chosen to lower the interfacial tension (IFT) between the brine/air proxy pair. The surfactant was chosen because even at very low concentrations it has a significant impact on the IFT value, while maintaining the viscosity value, thus allowing us to isolate potential effects of interfacial tension on trapping. Glycerol is

a water soluble visco-thickener used to alter the viscosity of the wetting fluid without significantly altering the IFT between the wetting fluid and non-wetting fluid.

All experiments with the altered wetting fluids (solutions containing Triton or glycerol) were paired with the same non-wetting fluid: air. Non-wetting fluids (octane and Soltrol) were paired only with the (unadulterated) 1:6 brine solution.

### 4.3 Experimental Set-Up

Experiments were conducted at standard temperature (22<sup>0</sup>C) and pressure (1 atmosphere). The sintered glass bead core was placed on top of a semi-permeable hydrophilic membrane (GE Nylon Membrane, 10 $\mu$ m) which prevented the passage of non-wetting fluid into the wetting fluid tubing lines. The core and filter paper were secured to a plastic base with a set of threaded, plastic connectors and an O-ring. The core holder design is shown in Figure 4.1

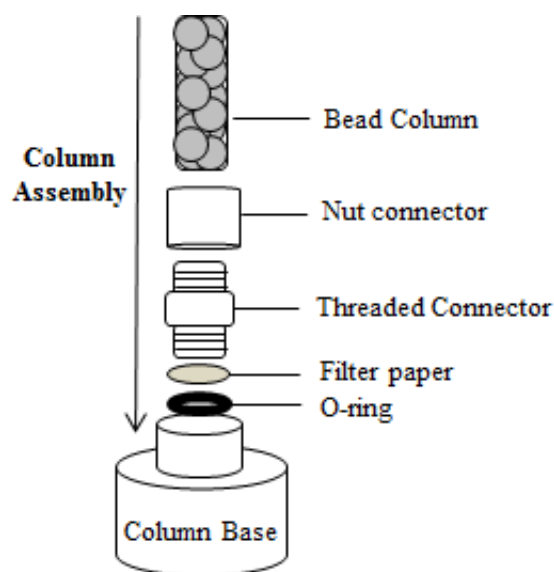


**Figure 4.1: A stacked schematic of the bead column experimental set-up.**

The bead core was connected to a system of Teflon tubing, pressure transducers and syringe pump. Two Validyne differential pressure transducers (22.5 cmH<sub>2</sub>O and 55.6 cmH<sub>2</sub>O capacity) were connected to the system apparatus to measure the capillary pressure and fluid equilibration within the bead column. Pressure measurements were collected throughout the entirety of each experiment. The transducers were calibrated at regular intervals.

A Harvard PhD Ultra Syringe pump precisely injected wetting fluid into the glass bead column during imbibition. The pump was reversed during drainage which displaced the wetting fluid by drawing in the non-wetting fluid from a reservoir connected to the top of the column. A schematic of the experimental set-up, depicting the described components, is provided in Figure 4.2.

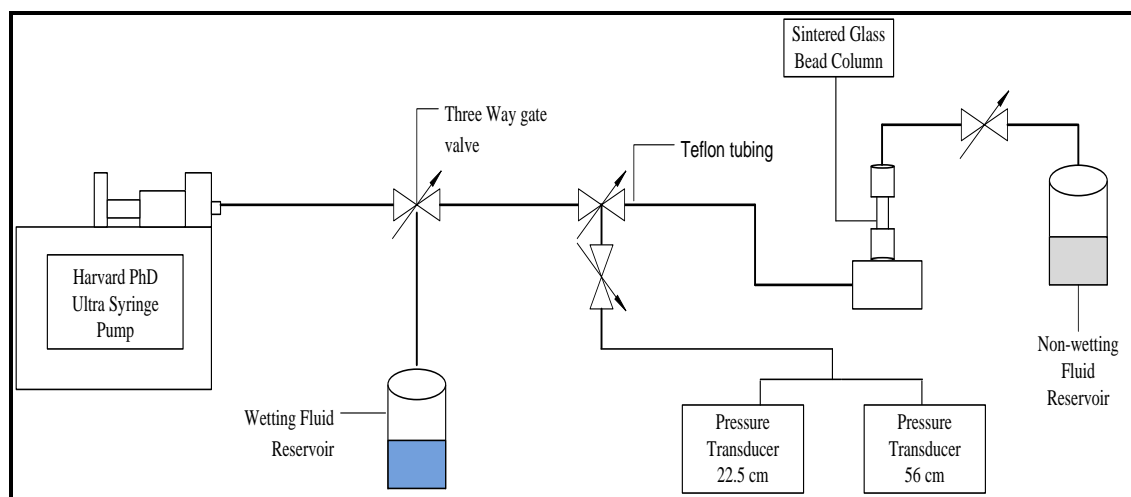


**Figure 4.2:** A schematic of the set-up used in all proxy fluid experiments.

#### 4.4 Experimental Procedure

The experimental set-up was assembled inside the hutch of a CMT scanner (Figure 4.3). Prior to each experiment, the glass bead column was removed from the experimental apparatus and cleaned with a series of fluids, each designed to dissolve and remove the preceding fluid from the column. The cleaning procedure required flushing the bead column first with acetone, then methanol, then deionized water, then dried with compressed air. This procedure was repeated prior to every experiment to ensure that the starting conditions were the same for each experiment.

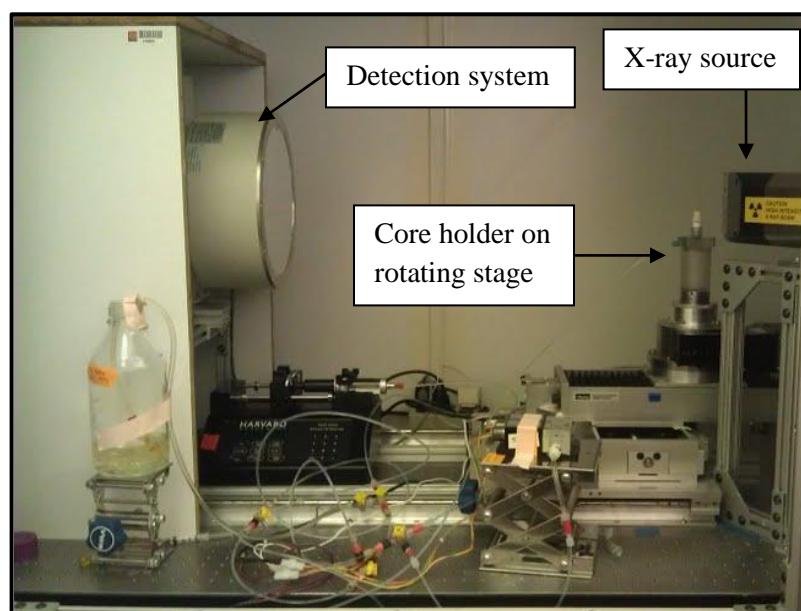


**Figure 4.3: The experimental set up inside the CMT scanner hutch.**

The clean, dry bead column was connected to the apparatus and secured onto the x-ray stage prior to the start of each experiment. The column was imaged in its dry state before fluid injection to simplify data processing.

All experiments were conducted over a series of three steps, which are summarized in Figure 4.4.

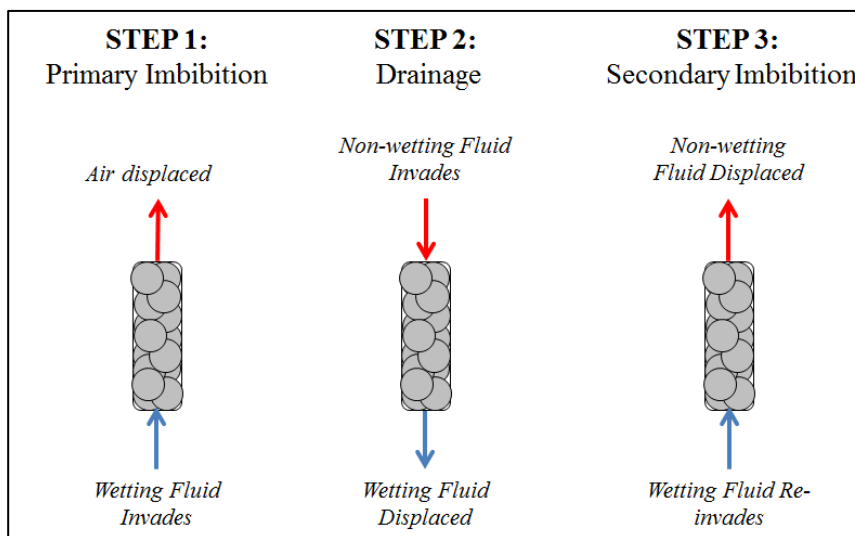


**Figure 4.4:** A summary of the three experimental steps: primary imbibition, drainage, and secondary imbibition.

After the dry scan, the first step involved injecting the wetting fluid into the column during primary imbibition (in which the wetting fluid displaced the non-wetting fluid). Primary imbibition was performed at a flow rate of 0.25 mL/hr to maximize complete saturation of the bead column without use of other measures such as vacuum. This process was complete once the wetting fluid reached the top of the beads and the pressure transducers indicated a capillary pressure of zero. The fluids in the column equilibrated for fifteen minutes after each pumping event. Once the column had equilibrated and the capillary pressure was approximately steady, the column was imaged again to measure the initial saturation in each experiment.

After the primary imbibition scan, the bead column was drained during the second step (drainage) at flow rate of 1 mL/hr. In experiments in which the non-wetting fluids were octane or Soltrol, a line of the non-wetting fluid was attached to the top of the bead column. When the

pressure transducers indicated by a negative spike in capillary pressure (at approximately -10 cmH<sub>2</sub>O) that the irreducible wetting fluid saturation ( $S_{irr}$ ) had been reached, the drainage process was stopped. After the equilibration period, the column was imaged again.

Once the drainage scan was complete, wetting fluid was re-imbibed into the column in the third step (secondary imbibition). Secondary imbibition fluid flow rates varied from 2-500 mL/hr. The secondary imbibition scan was initiated after a final 15 minute equilibration period.

## 4.5 Scanning

Images were collected using a CMT system (seen in Figure 2.5) constructed by Dr. Brian Bay in the School of Mechanical, Industrial and Manufacturing Engineering (MIME) at Oregon State University. The cone beam CMT system consists of a Focus FXE-160.20 x-ray tube, a Medelec 9" image intensifier (model: HXS-93/PS), and a 2448 x 2048 pixel 16 bit CCD Point Grey Grasshopper (model: GRAS-5055M) camera. The camera had a maximum resolution of 3.45 microns and a frame rate of 15 frames per second (fps). All experiments were operated at a voltage of 100 kilovolts (kV) and a current of 78 microamps ( $\mu$ A). Images were collected over a rotation of  $360^{\circ}$  in 1440 increments, averaging 4 projections per increment. The approximate spatial resolution of each image was 13 microns per pixel and the height of the imaged region of the bead column was 20 millimeters. This region varied slightly due to small changes in stage height between experiments.

## 4.6 Image Processing

### 4.6.1 Reconstruction

The images collected from each scan were saved in the form of two dimensional radiographs. The inherent image distortion of each 2D image was corrected using a distortion correction

algorithm in the Java-based program ImageJ. The distortion corrected 2D images of the dry, primary imbibition, drainage and secondary imbibition scans were reconstructed into three dimensional volumes using Octopus 8.5, an image reconstruction software program. Commercially available imaging software (Avizo™) was used to prepare the 3D volumes for further analysis.

#### 4.6.2 Segmentation

The goal of two fluid phase image processing is to convert the CMT collected grayscale images to images with three distinct phases (solid, wetting and non-wetting liquids) for quantitative analysis. Segmented images can be used to calculate a variety of desired system characteristics such as porosity, interfacial areas, and fluid saturations.

The first step in segmentation is registering (or aligning) the primary imbibition, drainage and secondary imbibition scans to the dry scan, such that the wetting and non-wetting fluid phases can be isolated from the glass beads which remain constant throughout each phase of the experiment.

After the images were registered, the reconstructed volumes were binarized to convert 16-bit grayscale images (with voxel values ranging from 0 to 65535) to segmented images in which each voxel is assigned a value of 0, 1 or 2, thus making the phases (and thereby wetting and non-wetting fluid saturations) more easily quantifiable.

First the upper and lower voxel boundaries of wetting and non-wetting fluids were defined. We refer to the dry scan as the “dry” volume and the primary imbibition, drainage and secondary

imbibition scans as the “wet” volumes. Figure 4.5 is a sample histogram containing voxel information from a corresponding dry and wet scan. Voxel values represent adsorption intensity and appear in the histogram according to the frequency in which they appear in each volume.

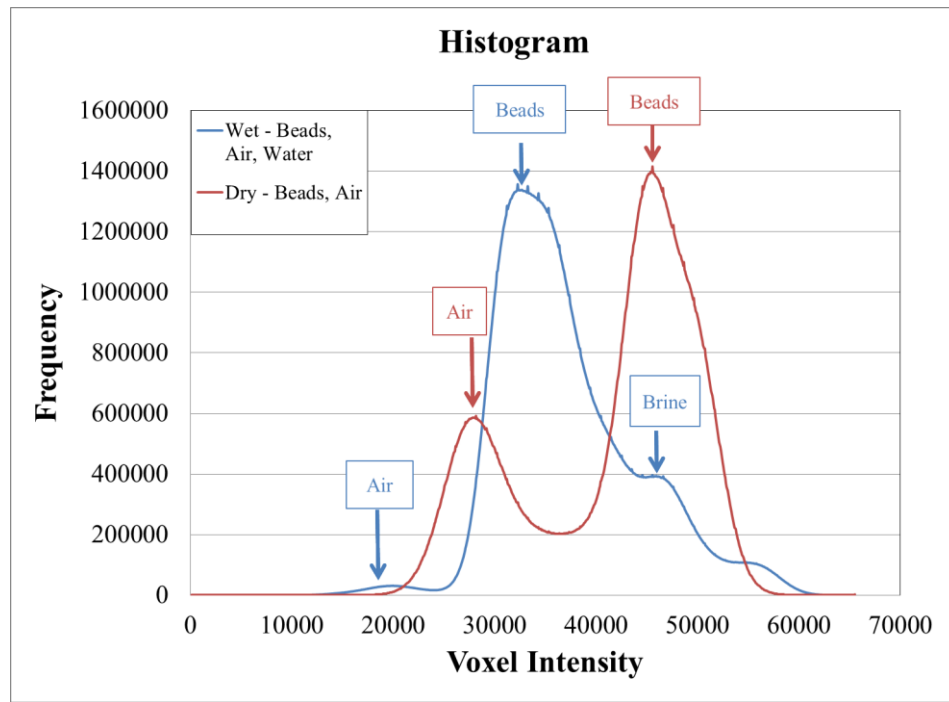


**Figure 4.5: Sample histogram containing voxel intensity values and the frequency in which they occur in a dry and wet grayscale volume.**

The dry volume, containing only non-wetting phase (air) and glass beads, has two distinct peaks, whereas the wet volume, containing non-wetting phase (air), wetting phase (brine) and glass beads, has three peaks on the histogram. The image threshold boundaries (i.e. binary limits) are associated with the first local minimums of each curve (at approximately 24000 and 39000 voxel intensity for the dry and wet scans, respectively in Figure 4.5). These minima were manually located and used to identify *only* the glass beads in the dry volume, and *all* of the

wetting phase and some of the glass beads in the remaining three wet volumes. This method, while overestimating the location of the local minima slightly, ensured that the non-wetting phase was completely isolated in both the dry and wet images, thus reducing the possibility of misidentified phases and error during segmentation and, ultimately, in the final results.

The volumes were median filtered prior to being binarized (i.e. post-thresholding) to remove noise in the data and segmented in the three distinct phases. Figure 4.6 (a) – (d) are image slices representing the segmentation process. The first two slices (a) and (b) are images from the dry and wet volumes after a filtering process. The subsequent two slices (c) and (d) are the resulting binarized images of the slices after thresholding. It is clear that all of the solid phase (glass) in slice (c) has been distinctly identified and only two phases are present: non-wetting phase (air) in black and solid phase (glass) in blue. The wet volume slice (d) has the non-wetting phase (air) identified in black and all of the wetting phase (brine) with a majority of the solid (glass) identified in blue.

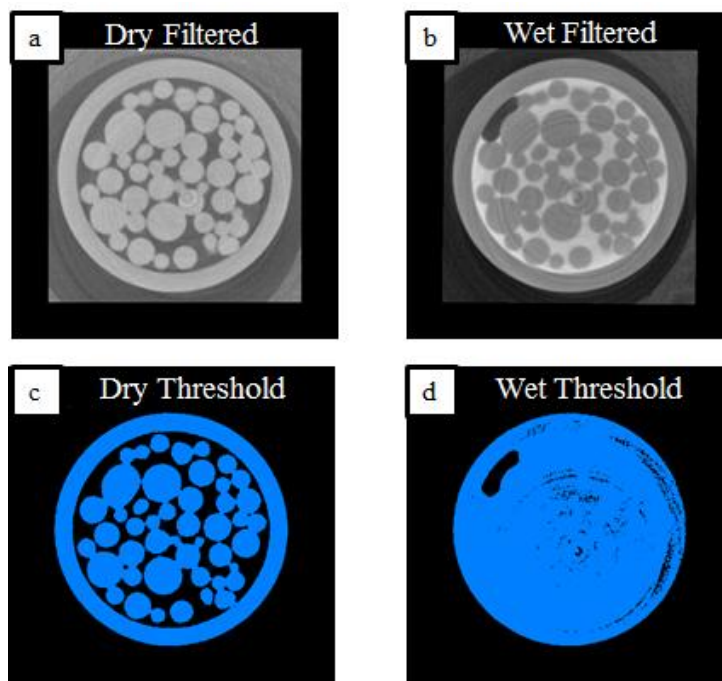


**Figure 4.6: Glass bead column slices during segmentation a) dry slice after image filtration, b) wet slices after image filtration, c) dry binarized slice and d) wet binarized slice.**

Once the dry and wet volumes were binarized, Figure 4.6 (c) and (d) were combined and each phase was assigned a value of 0, 1, 2 or 3, illustrated by Figure 4.7 (a). In this figure, the white streaks correlate to the falsely binarized areas in Figure 4.6 (d). These remain in Figure 4.7 (a) because they appear in both the dry and wet binarized images. The wet images are binarized such that all of the non-wetting (and wetting) phases are uniquely identified; therefore we know that the over-segmented voxels should be assigned a value associated with the solid phase (glass). The volumes are then processed to reassign over-segmented voxels (in white) to the correct value associated with the solid phase. A final segmented image with three distinct phases is produced and is shown in Figure 4.7 (b).

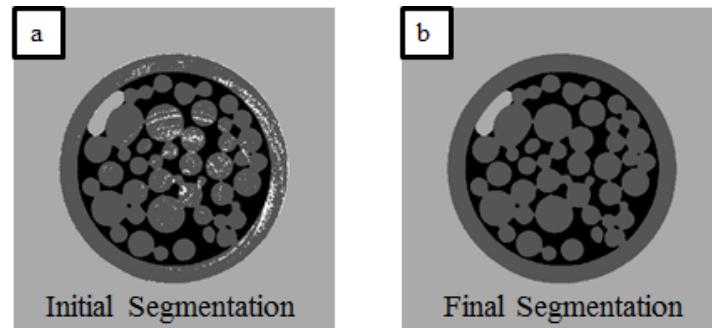


**Figure 4.7: Segmented volumes after a) initial segmentation with falsely binarized sections (white streaks), b) final segmentation with reassigned pixel values and three distinct phases.**

#### 4.6.3 Voxel Calculations

After segmentation, the extra space surrounding the glass column was removed from the image. The remaining pixels were labeled and the total number of voxels associated with each of the three markers: glass beads, wetting phase and non-wetting phase were calculated. The percent non-wetting saturation in the primary scan is defined as the original saturation,  $S_o$ , while the percent non-wetting saturation in the drainage scan is defined as the initial saturation,  $S_i$ , and the percent non-wetting saturation in the secondary imbibition is defined as the residual saturation,  $S_R$ .

The exact same region of the column was analyzed between the three scans within one experiment. However, this region changes somewhat due to height variation of the stage between experiments. The final calculated saturations from each scan represent approximately 10 mm of the total column.

## 4.7 Effects of Primary Imbibition

### 4.7.1 Initial Correlations and Reprocessing

A target goal of 98% original wetting saturation was set for each experiment; however data analysis of initial experiments indicated that this goal was not consistently achieved. A trend of increasing non-wetting phase saturation in the *secondary imbibition* scan with increasing non-wetting phase saturation in the *primary imbibition* scan emerged. Because so many CO<sub>2</sub> sequestration injection sites will consist of depleted oil reservoirs, this phenomenon is likely to be observed in the field and we chose to examine the effect, and correct for it, as opposed to trying to achieve full saturation (i.e. 100% saturation) for each S<sub>O</sub>.

Based on the apparent trend between the primary and secondary imbibition events, regions with the highest possible wetting saturation in the primary imbibition scans were identified. The wetting and non-wetting fluid saturations for each experiment were calculated over the re-analyzed region. Finally, the remaining original non-wetting saturations were subtracted from the residual non-wetting saturations, thus ensuring that true residual trapped non-wetting fluid was independent of the original non-wetting fluid. Figure 4.8 shows the trend of S<sub>O</sub> and S<sub>R</sub>, pre (left) and post processing corrections (right).

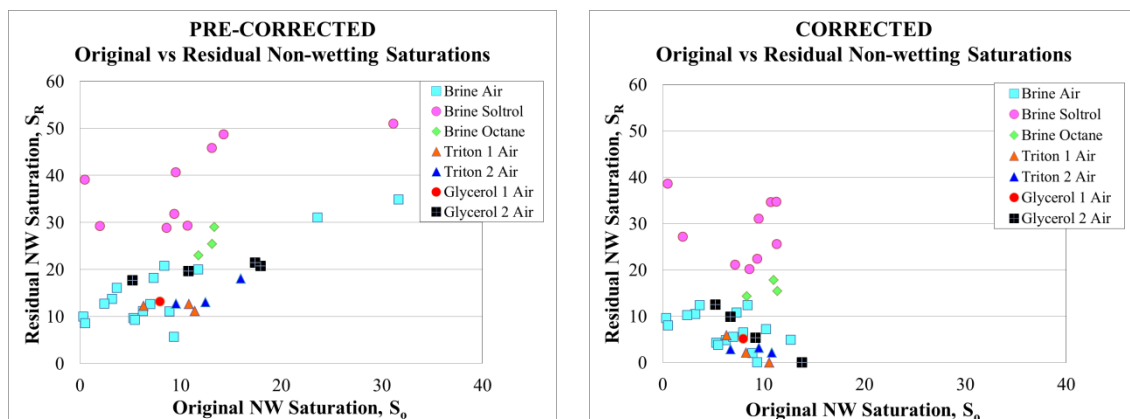


**Figure 4.8:** The relationship between *residual* non-wetting saturation and *original* non-wetting saturation prior to processing corrections (left) and after processing corrections (right).

An example of the steps taken during data processing is shown in the Avizo™ generated isosurfaces in Figure 4.9. Figure 4.9 (a) and (b) show the distribution of non-wetting phase obtained in a primary imbibition and secondary imbibition scan. The calculated original and residual non-wetting saturations are shown at the bottom of each isosurface. In this experiment, the primary imbibition scan did not meet the goal of at least 98% wetting saturation. Figure 4.9 (c) and (d) show the re-analyzed region of the column that was more fully saturated with wetting phase during primary imbibition. The scan in 4.9 (d) was subtracted from 4.9 (c) to produce 4.9 (e). Figure 4.9 (e) shows the true residual non-wetting phase saturation. These corrected values of  $S_R$ , which represent approximately 6.5 mm of the total column, are the values discussed in the results section in Chapter 5.

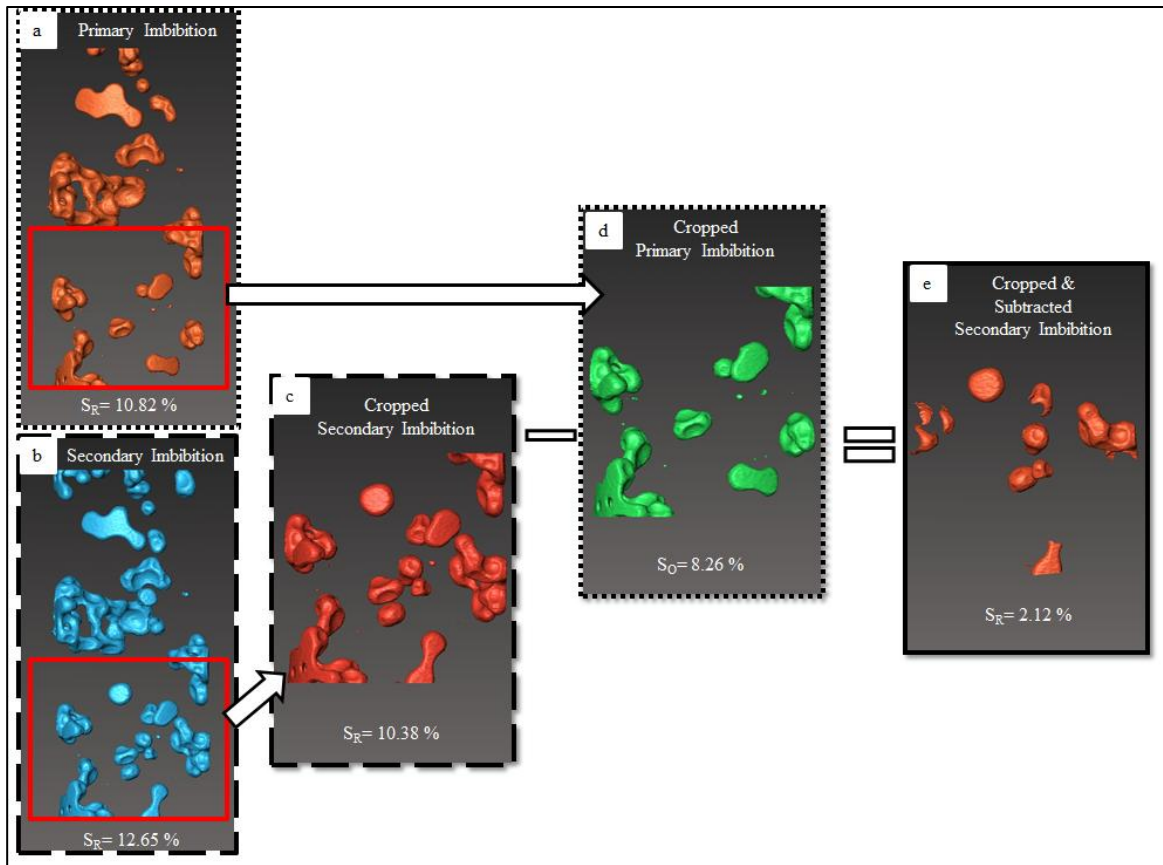


**Figure 4.9:** Avizo™ generated isosurfaces depicting residual saturation reprocessing steps.

#### 4.7.2 Primary Imbibition Dependence Quantification

The dependence of the residual non-wetting phase saturation on the original non-wetting phase saturation and the potential spatial correlation effects were quantified using Avizo™. The goal of this quantification process was to determine if the disconnected or immobilized voxels (blobs) of non-wetting phase trapped during primary imbibition,  $S_O$ , affected the amount and spatial arrangement of residual trapped phase,  $S_R$ .

The location of disconnected non-wetting phase blobs were separately identified in both the primary and secondary imbibition scans. The disconnected non-wetting blobs that did not appear in the same location in both scans were removed by subtraction. A new data set was

thus produced consisting of only the non-wetting phase disconnected blobs that appeared in both the primary and secondary imbibition scans. The ratio of the new data set to the disconnected non-wetting phase after secondary imbibition was defined as the “original saturation dependence”. In other words, the original saturation dependence is the percentage of residual non-wetting phase after secondary imbibition that is spatially correlated with isolated original non-wetting phase present after primary imbibition. A summary of the original saturation dependence based on each proxy fluid pair experiment is presented and discussed in the subsequent chapter.

## Chapter 5: Results and Discussion

The effects of primary imbibition wetting phase saturation and altered capillary number on the amount of trapped  $S_R$  are presented in this chapter. The experimental results are discussed in terms of their wetting/non-wetting fluid pairs. The experiments in which the **non-wetting phase** was altered are defined as Brine-**Air** (BA), Brine-**Soltrol** (BS), and Brine-**Octane** (BO). Altered **wetting** fluid (through addition of either the surfactant Triton100X or visco-thickener glycerol) experiments are defined as **Triton 1-Air** (T1A), **Triton 2-Air** (T2A), **Glycerol 1-Air** (G1A) and **Glycerol 2-Air** (G2A) in this chapter.

### 5.1 Dependence of Residual Saturation on Initial and Original Saturation

#### 5.1.1 Residual versus Initial Trapping

The dependence of trapped *residual* non-wetting phase on *initial* non-wetting phase has been well researched and summarized by Pentland et al., (2010), yet, to date only a few studies have addressed the pore-scale nature of this dependence. As discussed in Chapter 3, the resulting empirical trapping relationships provide a means of calculating *residual* non-wetting phase based on known *initial* non-wetting phase for both consolidated and unconsolidated media. Figure 3.2 depicts data from consolidated and unconsolidated media experiments in which a variety of proxy fluid pairs (air/water and oil/water) were utilized. The authors concluded that their initial and residual non-wetting saturations on unconsolidated sand packs followed slightly different empirical trapping curves; we would therefore expect our experiments on an unconsolidated bead pack to behave similarly. The *initial* and *residual* non-wetting saturations obtained during this work are plotted in Figure 5.1 and despite the differing media and fluid pairs, it is clear that our data exhibits similar residual trapping trends as reported for unconsolidated media by Pentland et al., (2010). As in Figure 3.2, the unconsolidated media

produce  $S_i/S_R$  relationships resulting in data points in the lower right-hand corner of the plot, i.e., relatively low  $S_R$  and fairly high  $S_i$  (<40%).

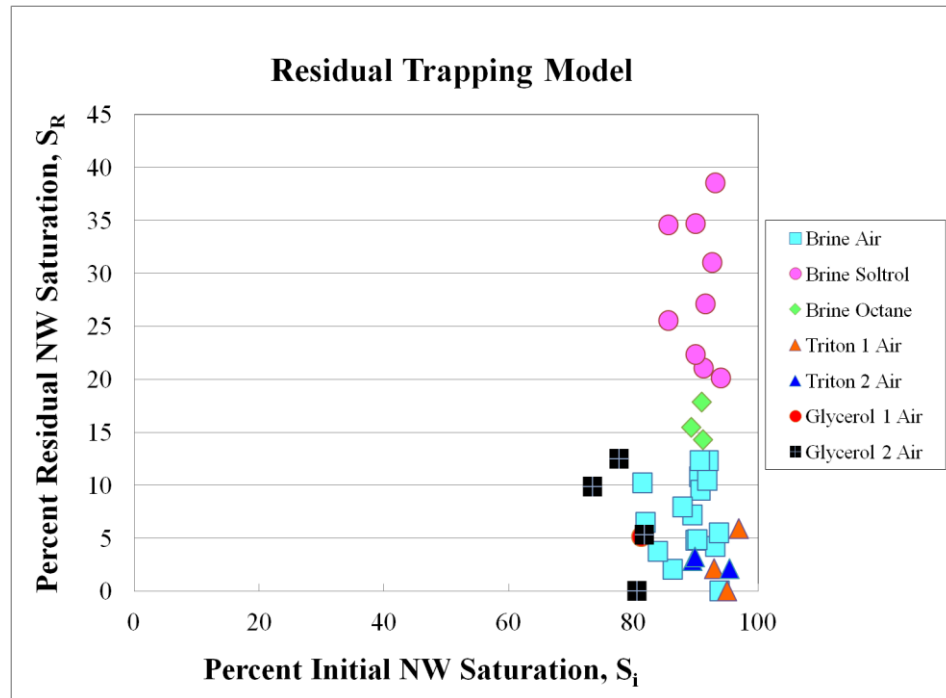


**Figure 5.1: Percent initial,  $S_i$ , and residual,  $S_R$ , non-wetting saturations from seven proxy fluid pairs.**

### 5.1.2 Residual versus Original Trapping

The dependence of *residual* trapped non-wetting phase on *original* non-wetting phase is not nearly as well characterized as the dependence of residual saturation on *initial* saturation. This is unsurprising given that, up until recently, most capillary trapping research has been aimed at enhanced oil recovery applications. With the new interest in geological CO<sub>2</sub> sequestration the focus has shifted towards optimizing capillary trapping mechanisms. To our knowledge, no research has been published that characterizes the relationship between non-wetting *residual* and *original* saturation. Figure 5.2 is the left side of Figure 4.7 revisited, which illustrates the relationship between  $S_O$  and  $S_R$  prior to any processing steps.

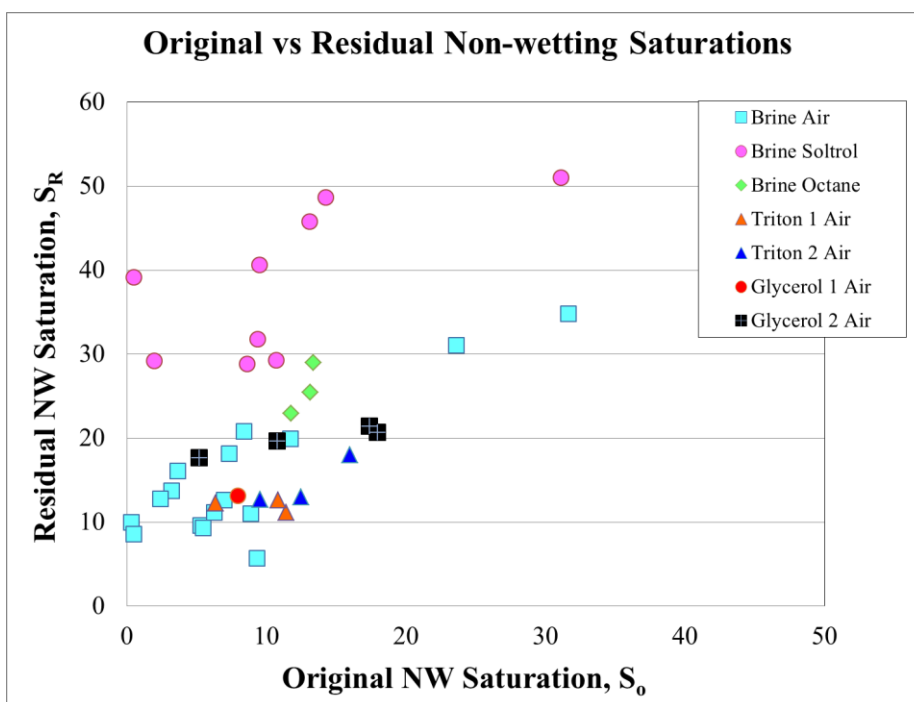


**Figure 5.2:** The relationship between *residual* non-wetting saturations,  $S_R$  and *original* non-wetting phase saturations,  $S_o$ , for all proxy fluid pairs.

As stated previously, Figure 5.2 shows a slight trend of increasing residual non-wetting saturation with increasing original saturation for all of the proxy fluid pairs. The BO and BS experiments are shifted upwards on the graph because of their increased trapping efficiency. At this point, further data analysis was necessary to quantify this observed trend.

The area of non-wetting phase that is spatially correlated, i.e. which appears in the same region of space within the bead column in both the primary and secondary imbibition scans, is defined as the “original saturation dependence”. The original saturation dependence indicates how much of an influence the immobilized (i.e. disconnected) original non-wetting phase has on the immobilized residual non-wetting phase. Figure 5.3 is a collection of three Avizo™ generated 3D isosurfaces that illustrate the original saturation dependence.

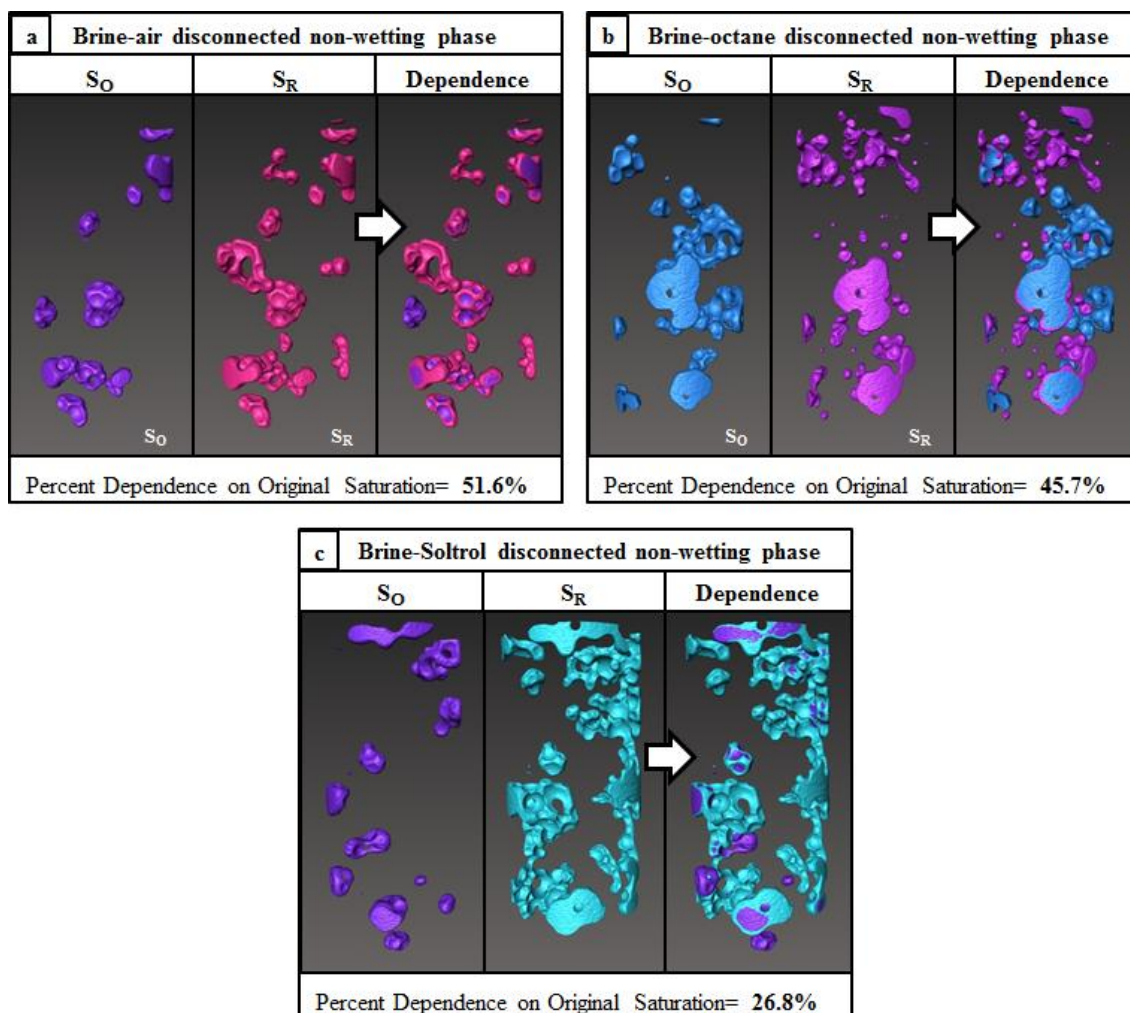


**Figure 5.3: Avizo<sup>TM</sup> isosurfaces depicting the percent original saturation dependence.**

The *original* immobilized non-wetting phase ( $S_O$ ) is represented by the blobs in the first panels of Figure 5.3 (a) – (c). While the *residual* immobilized non-wetting phase ( $S_R$ ) is represented by the blobs shown in each second panel. Finally, the percent  $S_O$  dependence is illustrated by an overlay of the first two panels in panel three. By calculating the ratio of redundant non-wetting volumes in each third panel to their respective non-wetting volumes in each second panel, we can quantify the  $S_O$  dependence. In the BA experiment, Figure 5.3 (a),  $S_R$  was approximately

52% dependent on  $S_O$ , for the BO experiment, Figure 5.3 (b),  $S_R$  was approximately 46% dependent on  $S_O$ , and in the BS experiment, Figure 5.3 (c),  $S_R$  was approximately 27% dependent on  $S_O$ . The  $S_R$  dependence on  $S_O$  for all the proxy fluids is plotted against their respective  $S_O$  values in Figure 5.4.

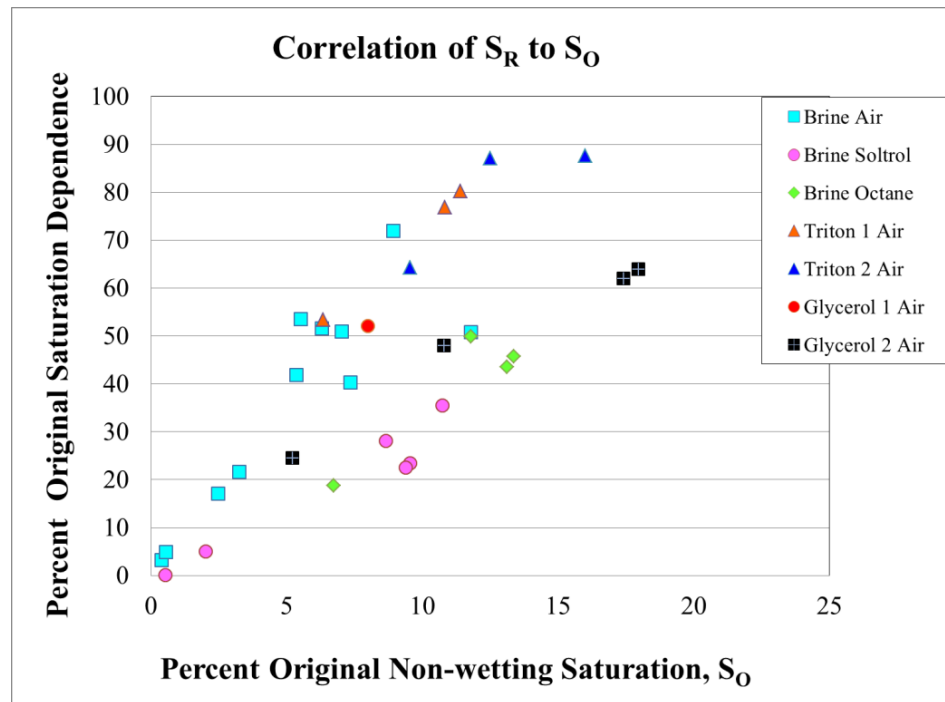


**Figure 5.4: Percent original non-wetting saturation dependence versus original non-wetting phase saturation for seven proxy fluid pair experiments.**

The data points shown in Figure 5.4 display an increasing correlation between  $S_R$  and  $S_O$  with increasing  $S_O$ . This trend provides a means of determining how influential the originally trapped non-wetting phase is on overall residual non-wetting phase trapping efficiency.

To better illustrate this dependence, Figure 5.4 was separated into four plots (Figures 5.5 and 5.6) which show the trends associated with the brine air, oil (octane and Soltrol), surfactant (Triton 1 and Triton 2) and visco-thickener (glycerol) fluid pairs.

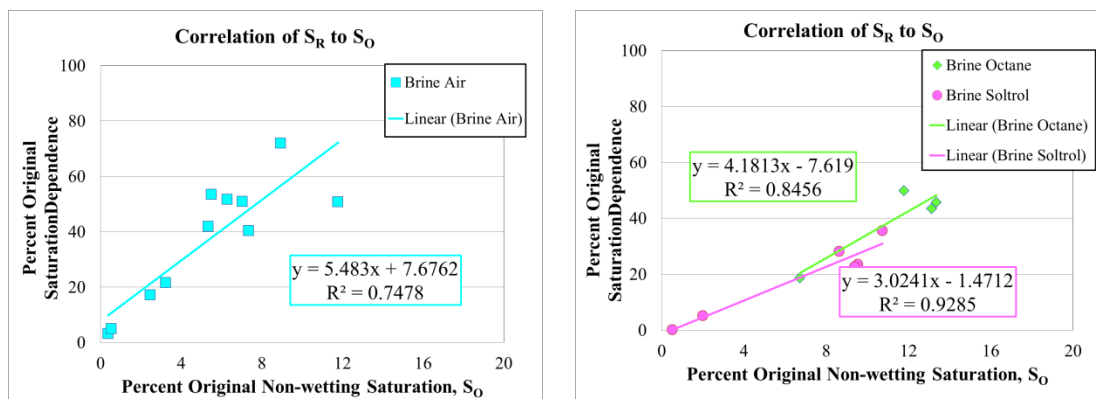


**Figure 5.5: Brine-air (left) and oil (right) experimental original saturation dependences plotted against their respective percent *original* non-wetting phase saturations.**

The brine-air experiments (Figure 5.5 left) and brine-oil experiments (Figure 5.5 right) exhibit linear regression lines, with  $R^2$  values for each of the three data sets above 75%. The BA experiments have original saturation dependences of 3%-72%. The Soltrol and octane data points appear slightly less dependent (with fewer data points) on the original trapped non-wetting phase saturations with percent dependence values ranging from 0%- 35% and 19%-50%, respectively.

The surfactant and glycerol data exhibit similar linear trend lines that suggest a relationship between increasing original saturation dependence and increasing  $S_O$ .

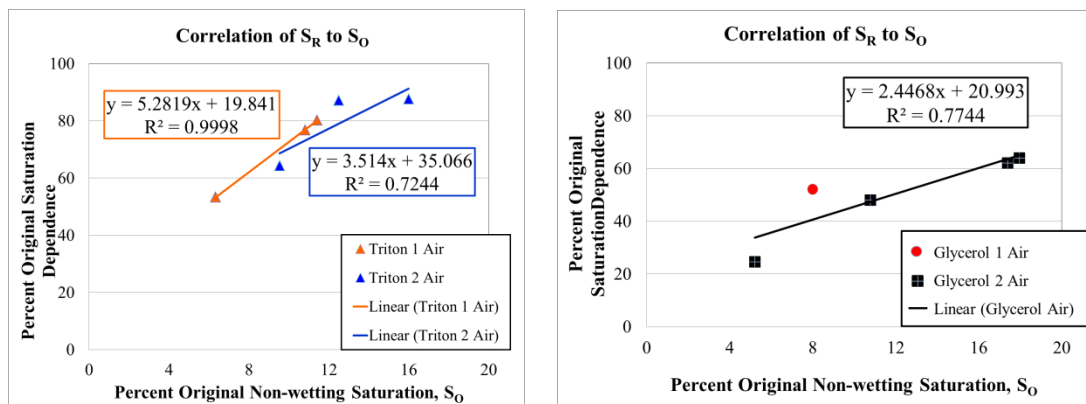


**Figure 5.6: Surfactant (left) and all glycerol (right) experimental original saturation dependences plotted as a function of percent residual non-wetting phase saturations.**

The surfactant data (Figure 5.6 left), particularly the T1A data points, have larger percent dependences on primary imbibition non-wetting phase with values ranging from 53%-80% and 64%-88%, respectively. The glycerol data (Figure 5.6 right), which combines both G1A and G2A experiments, has intermediate percent primary imbibition dependences ranging from 25%-64%. All the trend lines in both Figure 5.6 plots, like those in Figure 5.5, have  $R^2$  values greater than 70%. The magnitude of the slopes of all linear regressions along with their respective IFT and viscosity values, are listed in Table 5.1.

Table 5.1 Primary Imbibition Dependences						
Fluid Pair	$\sigma$ (dynes/cm)	$\mu_w$ (cP)	$\mu_{NW}$ (cP)	% $S_O$ Dependence	slope	$R^2$
Brine Air	72	1.13	0.018	3-72%	5.48	0.75
Brine Octane	37	1.13	0.54	19-50%	4.18	0.85
Brine Soltrol	25	1.13	4.82	0-35%	3.02	0.93
Triton 1 Air	37	1.13	0.018	53-80%	5.28	0.99
Triton 2 Air	50	1.13	0.018	64-88%	3.51	0.72
Glycerol Air	66 – 69	1.86 – 3.95	0.018	25-64%	2.45	0.77

The information summarized in Table 5.1 is important because it indicates, through a linear regression analysis, that *residual* non-wetting phase trapping is highly dependent on the original non-wetting phase present in the pore space. Specifically, a relationship between the magnitude of the linear  $S_O$  slopes on fluid (both wetting and non-wetting phase) viscosity is evident. The glycerol solutions have the highest *wetting* phase viscosities (1.86 – 3.95 cP) and the lowest dependence on the original saturation (with a slope of 2.45). The BA, BO and BS data indicates that increasing *non-wetting* phase viscosity (from 0.018 – 4.82 cP) results in a decreased dependence on original saturation (with slopes from 5.48 – 3.02, respectively).

The original non-wetting saturation for each experiment represents the amount of *air* trapped in the pore space during primary imbibition. During secondary imbibition when the wetting fluid displaces the non-wetting fluid (air, octane, Soltrol), non-wetting fluids octane and Soltrol can more easily remove the originally trapped air during their displacement due to their high viscosities. Correspondingly, in experiments in which air is the non-wetting phase, the glycerol wetting fluid can more easily dislodge the trapped air from the pore space during secondary imbibition because of its increased viscosity. Thus, we would expect to see a trend of decreasing original saturation dependence with increasing non-wetting *and* wetting fluid viscosity.

Information about pre-existing non-wetting phase (e.g. oil in deplete oil reservoirs or gas in saline aquifers) might prove valuable in terms of estimating trapping capacity in field applications. Since both wetting phase and non-wetting phase viscosity affects the dependence of injected fluid on in-situ (original) fluid, alterations can be made to the viscosity of

supercritical CO<sub>2</sub> or a chase water flood to increase the efficiency (i.e. the volume of gas stored) of a CO<sub>2</sub> sequestration project.

## 5.2 Residual Trapping Results

### 5.2.1 Summary of Capillary Number Effects

For this analysis, capillary numbers (eq. 2.4) are calculated based on secondary imbibition events but also represent fluid properties associated with the invading (in our case, the wetting) fluid. The capillary numbers for experimental results in this work range from approximately  $10^{-3}$  to  $10^{-6}$ . Research has shown that as capillary numbers increase, viscous forces dominate, resulting in a decrease in residual non-wetting phase trapping which is generally exhibited as a dramatic decrease in  $S_R$  around capillary numbers  $10^{-5}$  to  $10^{-6}$  (Chatzis and Morrow, 1984; Morrow et al., 1988; Ding and Kantzas, 2007; Cense and Berg, 2009) and is illustrated in Figure 3.3. However, this expected trend was not observed in our experimental results; see Figure 5.7 which shows capillary numbers and the corresponding *residual* non-wetting phase saturations,  $S_R$ . In general, higher  $S_R$  is observed for higher non-wetting phase viscosities, but otherwise no real trend can be discerned from the data.

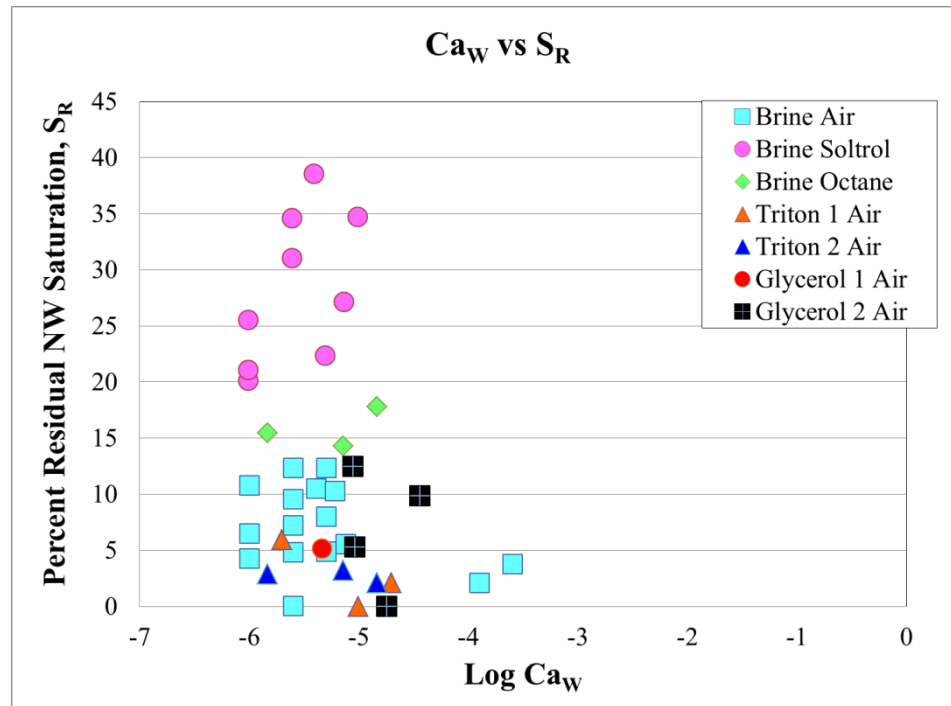


**Figure 5.7:** Capillary numbers based on the invading fluid (*wetting-phase*) properties for the seven proxy fluid pairs plotted against their resulting *residual* non-wetting phase saturation.

This lack of trend between capillary number and residual saturation can be due to a number of reasons. First, most published research on this topic has been aimed at enhanced oil recovery applications. Oil recovery differs from CO<sub>2</sub> sequestration in that in oil recovery the goal is to maximize mobilization of non-wetting phase (oil), rather than to maximize the amount of trapped injected non-wetting phase (CO<sub>2</sub>) within the pore space. The alternate capillary number, representing properties of the non-wetting fluid phase, is often used in oil recovery research. The non-wetting phase-based capillary numbers for the experiments presented here range from 10<sup>-4</sup> to 10<sup>-8</sup> and are shown in Figure 5.8.

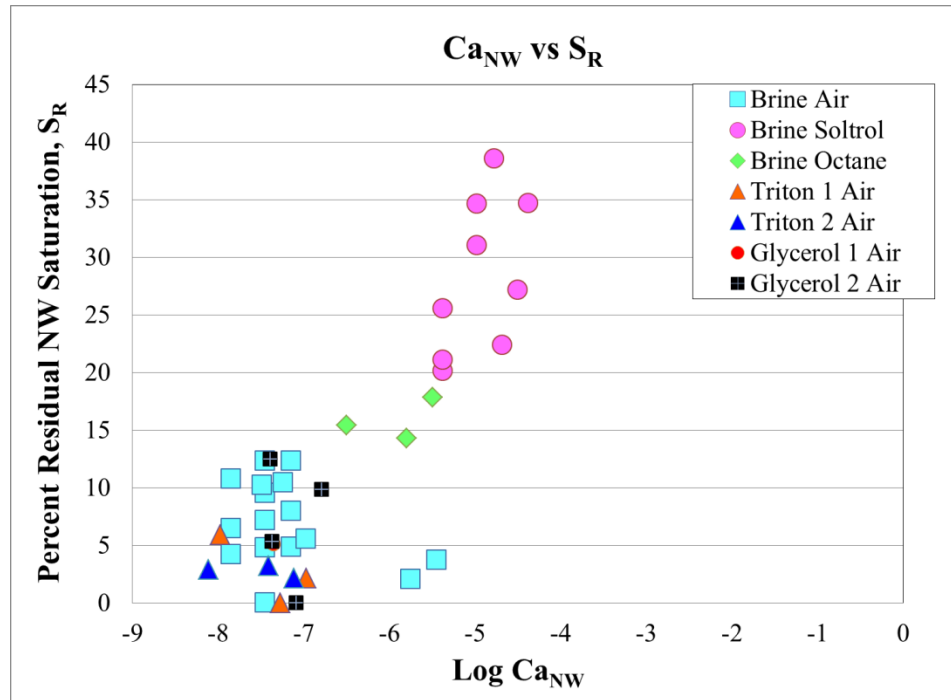


**Figure 5.8:** Capillary number based on properties of the displaced fluid (*non-wetting-phase*) for the seven proxy fluids plotted against their resulting *residual* non-wetting saturations.

The two BA experiments with the largest capillary numbers ( $10^{-6}$ ) in Figure 5.8 have significantly lower residual non-wetting saturations than their BO and BS capillary number counterparts, thus disproving a potential trend of decreasing  $S_R$  with increasing non-wetting phase capillary number. Therefore, the definition of capillary number is not the source of the non-conformity as compared to established capillary number versus  $S_R$  trends.

Another reason for the lack of a relationship between capillary number and residual trapping could be that our experiments were conducted on unconsolidated glass bead packs, while most published data represents consolidated rock cores, typically sandstone (Chatzis and Morrow, 1984; Chatzis et al., 1988; Kantzas et al., 2001; Ding and Kantzas, 2007; Bachu and Bennion, 2008; Suekane et al., 2009; Shen et al., 2010). Residual non-wetting phase trapping in high porosity, unconsolidated media does not follow the same trends as consolidated media

(Pentland et al., 2010). The small pores in highly consolidated media allow for non-wetting phase to invade and remain trapped by capillary forces in the pore space to a greater extent than in unconsolidated media. Additionally, our unconsolidated glass bead cores comprise an idealized pore structure and could behave differently from unconsolidated media extracted from natural systems (e.g. sand packs). Morrow et al., (1988) presented sintered bead pack capillary trapping data that indicated a decline in residual trapped oil with increasing capillary number (based on the viscosity of the wetting fluid) over a narrow range of capillary numbers,  $10^{-4}$ - $10^{-3}$ . Our work did not include experiments at such high capillary numbers, thus additional experimentation is necessary to compare to these results. However, it should also be noted that the Morrow et al., (1988) experiments involved mobilizing trapped oil, not immobilizing trapped CO<sub>2</sub>, which is the ultimate goal of our work.

### 5.2.2 Impact of Flow Rate

Despite the lack of trends, Figures 5.7 and 5.8 do provide valuable insight into the elements of capillary number and its potential effect on trapping. We observe three distinct clusters in the data points in both figures. The first cluster, with the highest percent residual saturations (~20-40%), consists of the BS data points. Following the BS data points are the BO data points with intermediate trapping results with approximately 15-20% residual non-wetting saturation. The final cluster is a mix of the remaining proxy pairs (BA, T1A, T2A, G1A and G2A) data with low residual trapping saturations (0-15%). The residual saturations are generally higher than published residual saturation in glass bead packs, which reported maximum residual non-wetting saturations of approximately 3.5% for a water-nitrogen gas system (Suekane et al., 2010) and 16% for a water-oil system (Morrow et al., 1988).

The grouping of  $S_R$  values is a result of alterations made to the properties investigated in this work: fluid flow rate, interfacial tension, and/or viscosity.  $S_R$  as a function of secondary imbibition flow rate (2-20 mL/hr) for each fluid pair are plotted in Figure 5.9.

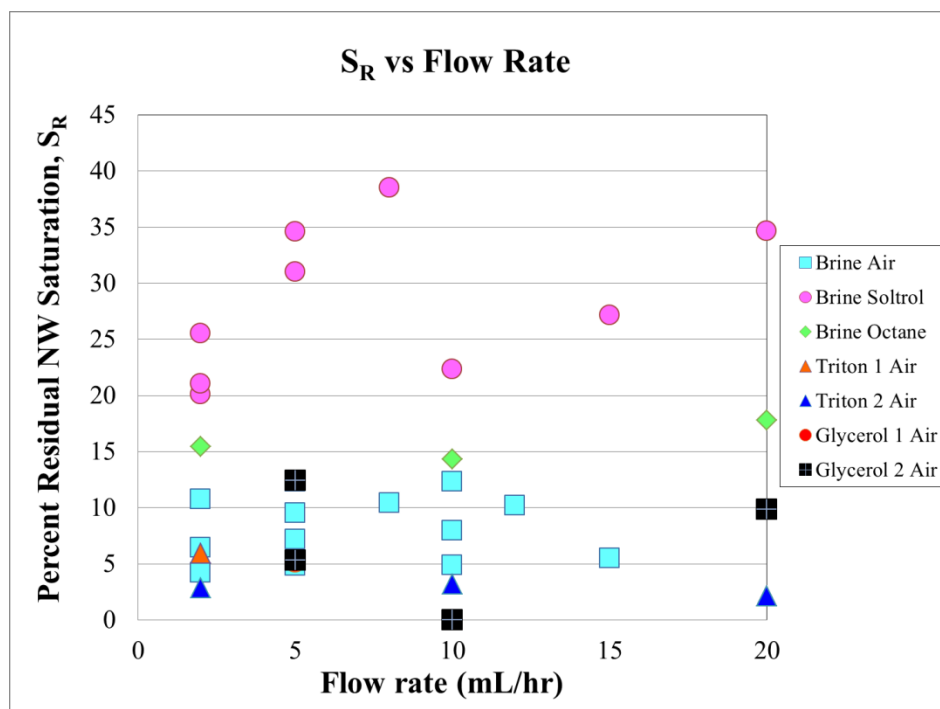


**Figure 5.9: Residual non-wetting phase trapping,  $S_R$ , for seven proxy fluid pairs as a function of secondary imbibition flow rate.**

BS experiments, as shown in previous figures, exhibit the highest residual saturations, followed by BO data points then BA, T1A, T2A, G1A and G2A data points. Within each fluid pair there does not appear to be any dependence of residual saturation on flow rate that exceeds the scatter in the data. Wildenschild et al., (2011) found a weak trend with non-wetting flow rate for all fluid pairs. However, the  $S_R$  values remained relatively low for all proxy fluids in their experiments and their highest flow rate was 10 mL/hr. The main difference between the setup of

Wildenschild et al., (2011) and the present work is that the glass bead core was sintered to the core holder, thus eliminating any potential sidewall flow effects.

To further explore the effects of flow rate, two additional BA experiments were conducted at 250 and 500 mL/hr, two orders of magnitude higher than the slowest experimental flow rate (2 mL/hr). The residual saturations associated with these flow rates are plotted with the rest of the BA experiments in Figure 5.10.

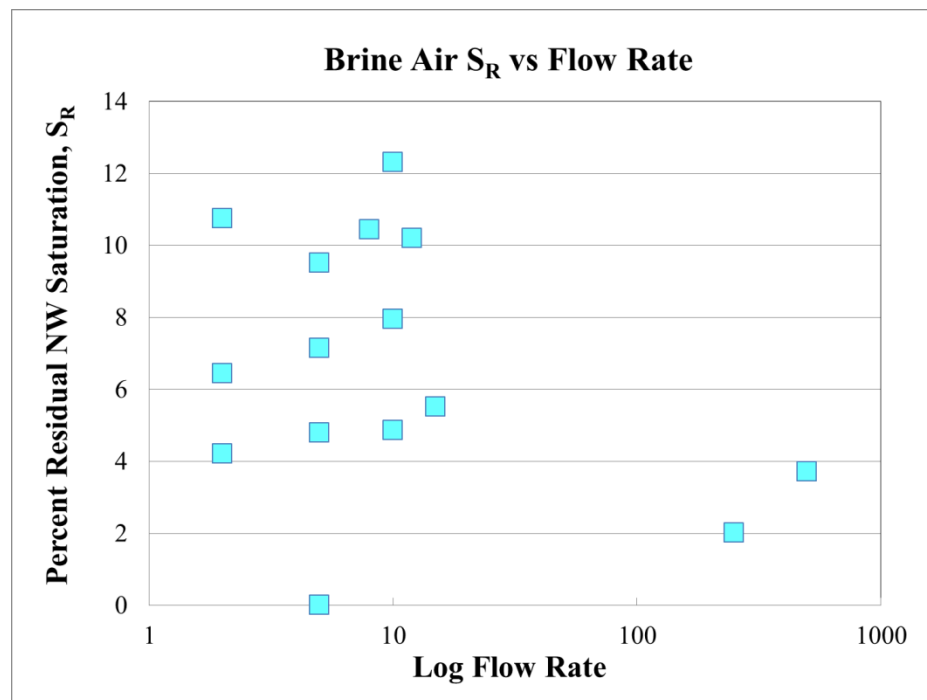


**Figure 5.10:** Percent residual non-wetting saturations,  $S_R$ , plotted against secondary imbibition flow rate including the two additional flow rates at 250 mL/hr and 500 mL/hr.

As illustrated in Figure 5.10, the BA data points at 250 and 500 mL/hr are slightly lower than most of the other data points; yet no substantial trend can be discerned.

To further explore flow rate effects, Avizo<sup>TM</sup> generated 3D isosurfaces were used to visualize fluid interactions at the pore-scale. The three isosurfaces shown in Figure 5.11 represent BO experiments conducted at 2, 10 and 20 mL/hr.

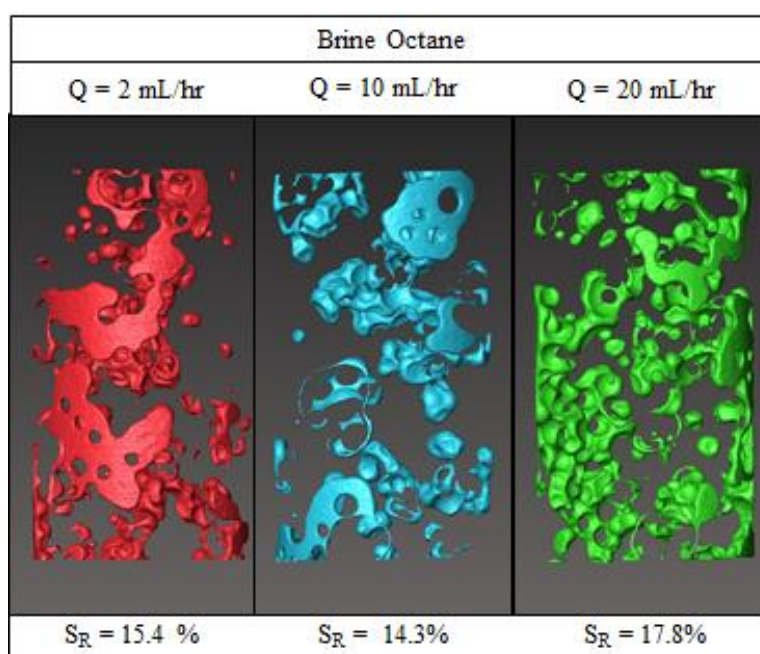


**Figure 5.11: Three Avizo<sup>TM</sup> isosurfaces representing trapped non-wetting fluid from brine-octane experiments conducted over a range of secondary imbibition flow rates of 2-20 mL/hr.**

The residual saturations from the three BO experiments are fairly similar over the three secondary imbibition flow rates with an average saturation of approximately 16%. Thus, the BO data shows a very tentative increase in trapping with flow rate with a local minimum at 10 mL/hr, but the scatter in the data makes it difficult to draw a solid conclusion regarding flow rate effects in general. Despite published research that proposes an inverse relationship between flow rate and residual trapped non-wetting phase (e.g. Blunt and Scher, 1995; Nguyen et al., 2006), we suggest that residual non-wetting phase trapping is not dependent on fluid flow rate in the glass bead material.

### 5.2.3 Interfacial Tension Effect

The effect of IFT on residual trapping was explored by the addition of surfactant to the wetting fluid (brine) solution. The surfactant was chosen because it would not alter the wetting phase viscosity, thus isolating potential IFT trapping effects. IFT values for the seven proxy fluid pairs were altered over a range of 25 – 72 dynes/cm. The measured  $S_R$  values at these IFTs are shown in Figure 5.12.

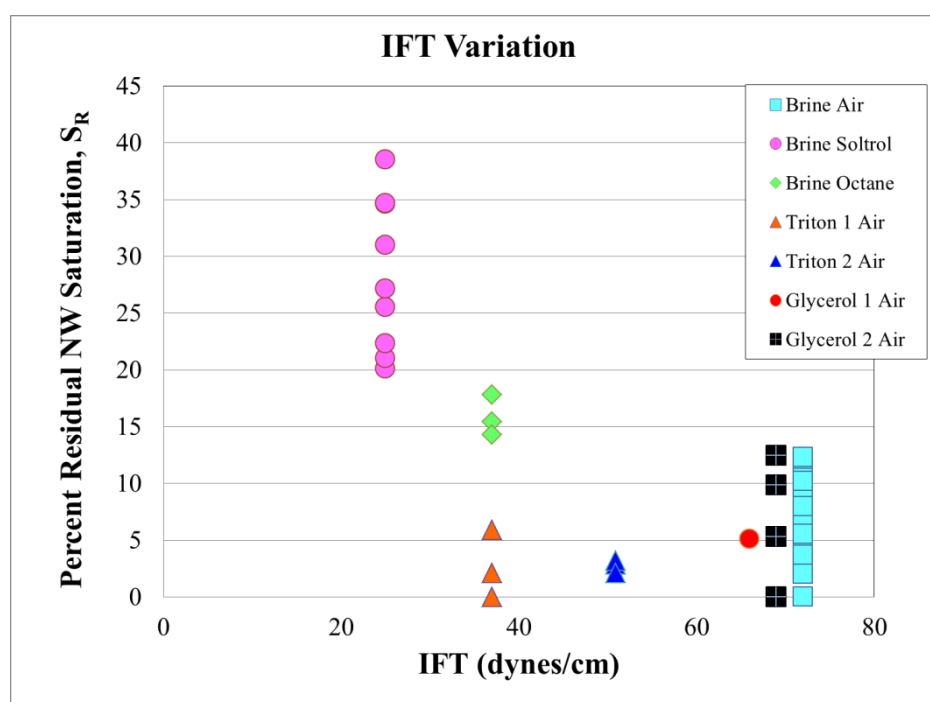


**Figure 5.12: Interfacial tension variation for the seven proxy fluid pairs plotted against percent residual non-wetting phase saturation.**

At first glance, a distinct decreasing trend in the  $S_R$  with increasing IFT appears; this same trend was also found by Wildenschild et al., (2011). However, the BS and BO experiments consist of proxy fluid pairs where not only IFT, but also viscosity has been altered. The BS fluids had the lowest interfacial tension (25 dynes/cm) and highest overall percent residual trapping at 38%. The T1A, T2A, G1A and G2A experiments have IFT values that vary by about a factor of two,

but produced similar residual saturations, in the range of 0-13%. The BO fluid pair resulted in intermediate residual saturation percentages of 14-18%. The BO experiments and T1A experiments had exactly the same IFT value (37 dynes/cm), but exhibited distinctly different residual non-wetting saturations as shown in Figure 5.13, which contains 3D isosurfaces for two of the three BO and T1A experiments after secondary imbibition. The fluid depicted in each column is the residual non-wetting fluid (octane and air).

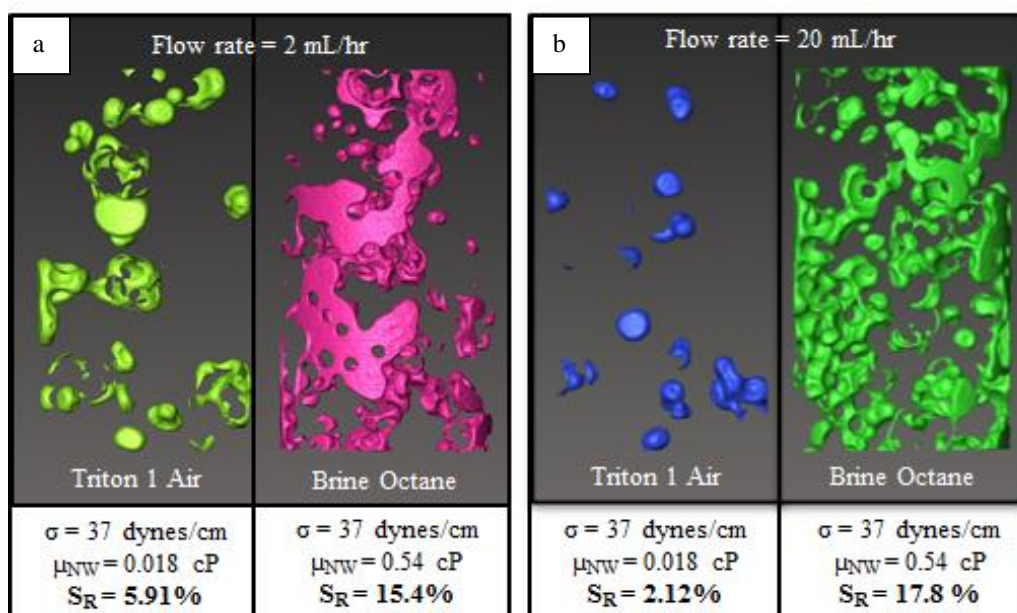


**Figure 5.13: Interfacial tension  $S_R$  comparison for (a) flow rate of 2 mL/hr and (b) flow rate of 20 mL/hr, for T1A and BO experiments.**

The isosurfaces show distinct differences in trapped amount and spatial arrangement for the two fluid pairs.  $S_R$  values of 5.91% and 15.4% at 2 mL/hr were obtained for the T1A and BO experiments, respectively. The same trend was seen at 20 mL/hr with measured  $S_R$  values of 2.12% and 17.8%, respectively. If IFT controlled residual trapping then we would expect fluid pairs with the same IFT to produce similar non-wetting phase saturations, however this was

clearly not the case. Additionally, according to Laplace's Law (eq. 2.3) capillary pressure is proportional to IFT, and increasing capillary pressure would make it more difficult for the wetting fluid to invade pores during secondary imbibition, thus more non-wetting phase will remain in the pore space. We clearly did not observe this trend, and conclude that variations in residual saturations over the ranges of IFT used are more likely caused by the change in viscosity, as described in the following section.

#### 5.2.4 Effect of Viscosity Changes

Viscous effects are unique from the other two elements of capillary number (flow rate and IFT) in that the wetting fluid and the non-wetting fluid can both be made more and less viscous, independently.

##### 5.2.4.1 Wetting Fluid Viscosity

Glycerol was added to the brine solution to isolate the impact of *wetting* fluid viscosity on residual trapping. Two glycerol solutions (G1A and G2A) were prepared with viscosities that were approximately a factor of two and a factor of four times greater than the original brine solution, respectively. Figure 5.14 shows the wetting phase viscosities and the resulting  $S_R$  values.

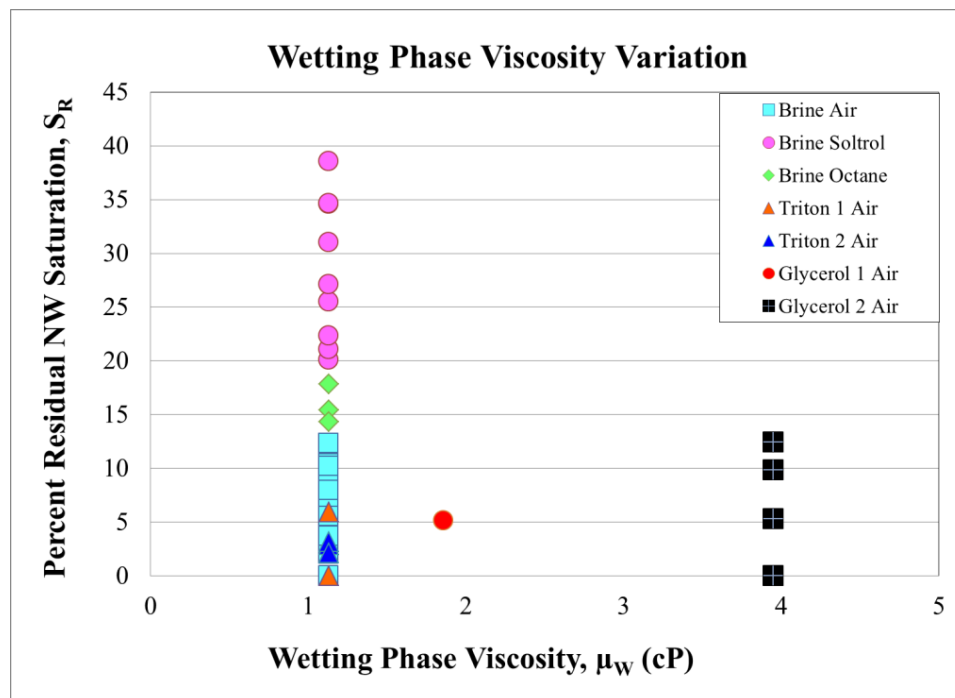


**Figure 5.14: Proxy fluid pair data plotted in terms of wetting fluid viscosities against percent residual non-wetting saturations.**

The BA, BS, BO, T1A and T2A experiments all had wetting phase viscosities of 1.13 centipoise (cP). The G1A experiment had a viscosity of 1.86 cP and a corresponding  $S_R$  of 5.10%, while the G2A experiment had a viscosity of 3.95 cP and  $S_R$  values that ranged from 0-12.4%. Figure 5.14 shows that altering the wetting phase viscosity (by factors of two and four) does not increase trapping, i.e., the two glycerol solutions have a similar effect on residual trapping as the original brine solutions. The only discernible effect is from changes in non-wetting phase viscosity, resulting in  $S_R$  values of up to 38% for BS data points. Non-wetting phase viscosity appears to be a controlling factor for optimizing  $S_R$  and is further discussed below.

#### 5.2.4.2 Non-wetting Fluid Viscosity

Three non-wetting fluids with differing viscosities were used in this research. These viscosities increased by an order of magnitude starting first with air at 0.018 cP, octane at 0.54 cP and

ending with Soltrol at 4.82 cP. The  $S_R$  values are plotted against these non-wetting phase viscosities in Figure 5.15.

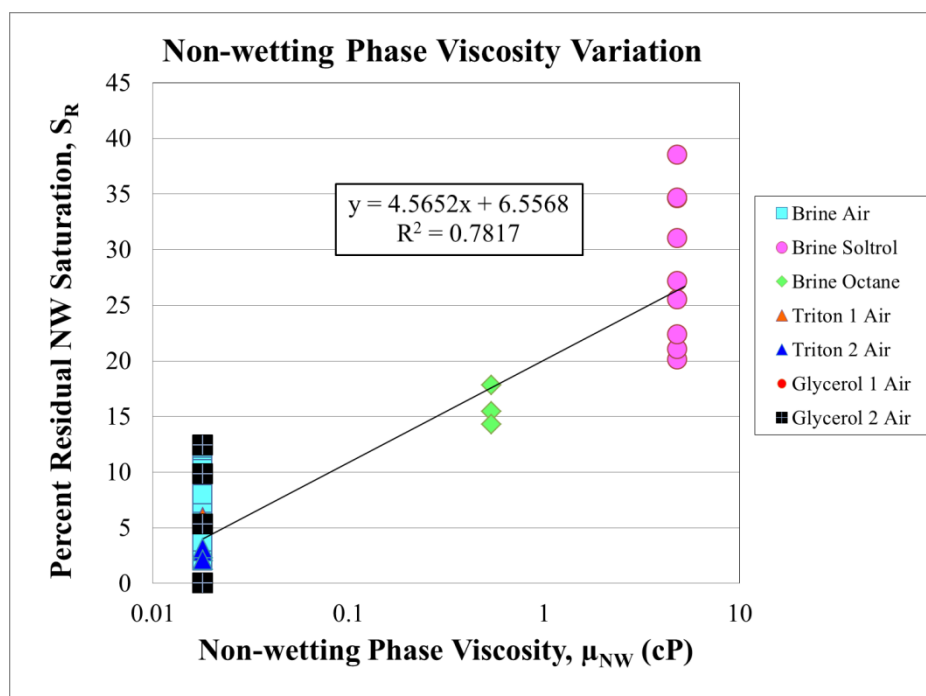


**Figure 5.15: Residual non-wetting phase saturations versus non-wetting phase viscosities for the seven proxy fluids.**

All of the proxy fluid pairs using air as the non-wetting fluid (BA, T1A, T2A, G1A and G2A) have residual non-wetting saturations that range from 0-12.4%. Next the three BO experiments have distinctly higher residual saturations that range from 14.3-17.8%. At the highest non-wetting phase viscosity, the BS experiments have residual non-wetting saturations that vary from 21-38.5%. Despite some noise in the data, a distinct trend, confirmed by the  $R^2$  value of greater than 75%, of increasing non-wetting phase residual saturation with increasing non-wetting phase viscosity is observed.

To further illustrate this observed trend, isosurfaces were created for the different non-wetting phase viscosities. Figure 5.16 shows trapped non-wetting phase in the three columns after secondary imbibition at 2 mL/hr in BA, BO and BS experiments. The residual saturations increase from 4.20% for BA to 20.9% for BS with increasing non-wetting phase viscosity.

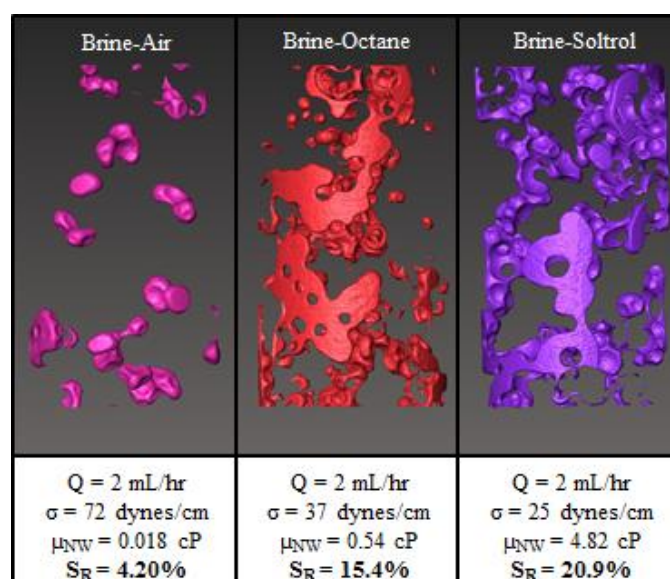


**Figure 5.16:** Trapped residual non-wetting phase after secondary imbibition at 2mL/hr for proxy fluid pairs BA, BO and BS.

Further support of this relationship between increasing *non-wetting phase* viscosity and non-wetting phase residual saturation is provided by revisiting Figure 5.13. In this figure, 3D isosurfaces of residual non-wetting phase associated with T1A and BO experiments, which were conducted at identical flow rates and IFTs, were compared. The residual saturations from the BO experiments, with an order of magnitude larger non-wetting phase viscosity, are 10 - 15% higher than the T1A experiments. Our sequence of experiments has thus eliminated significant effects on  $S_R$  values from any other variable than *non-wetting phase* viscosity.

Relatively little is known about the relationship between non-wetting phase viscosity and residual trapping. Recent research has explored the effect of viscosity on trapping in the form of mobility ratio (eq. 2.5), the ratio of the wetting and non-wetting fluid viscosities (Bachu and Bennion, 2008). Published trends indicate decreased residual trapping with an increasing mobility ratio (Bennion and Bachu, 2005). Bachu and Bennion (2008) argue that as the mobility ratio increases (lowering the non-wetting phase viscosity), the dominating wetting fluid experiences less resistance while flowing in the pore space. In these instances, the wetting phase is more likely to dislodge non-wetting phase, but also prevent non-wetting phase immobilization at high mobility ratios.

Table 5.2 Experimental wetting and non-wetting fluid viscosities				
Wetting Fluid	Non-wetting Fluid	$\mu_w$ (cP)	$\mu_{NW}$ (cP)	M ( $\mu_w / \mu_{NW}$ )
Brine	Air	1.13	0.018	62.8
Brine	Soltrol	1.13	4.82	0.2
Brine	Octane	1.13	0.54	2.1
Triton 1	Air	1.13	0.018	63.1
Triton 2	Air	1.13	0.018	63.1
Glycerol 1	Air	1.86	0.018	102.3
Glycerol 2	Air	3.95	0.018	218.8

Mobility ratios calculated from the wetting and non-wetting fluid viscosities are summarized in Table 5.2 and plotted against  $S_R$  in Figure 5.17.

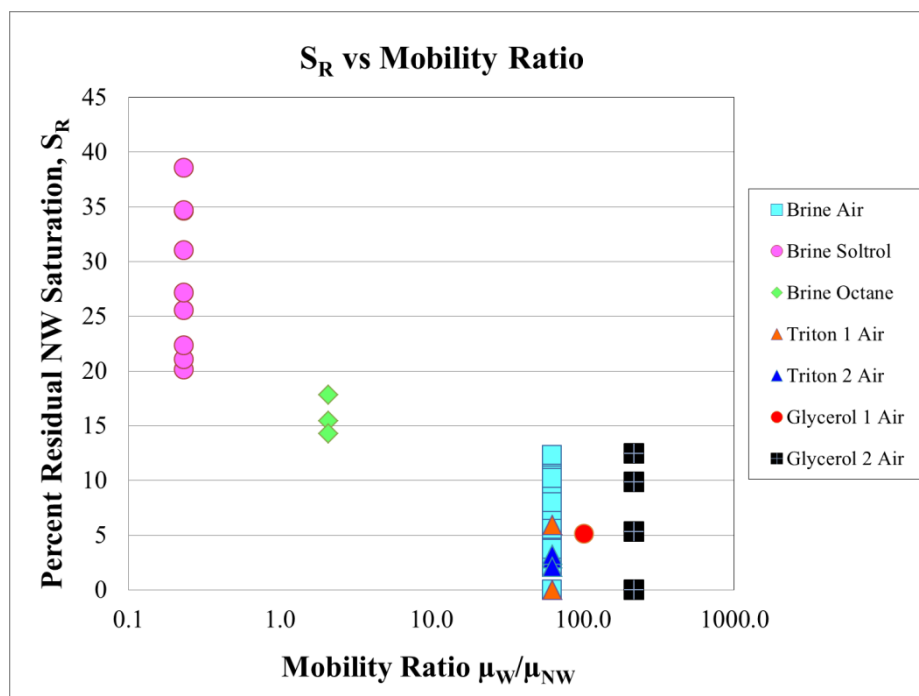


**Figure 5.17: Experimental mobility ratios ( $\mu_w/\mu_{NW}$ ) for the seven proxy fluid pairs are plotted as a function of their respective residual non-wetting phase saturations.**

Table 5.2 and Figure 5.17 depict mobility ratios that range from approximately 0.2 to 220. Figure 5.17 supports the trend of increasing residual saturation with decreasing mobility ratio thus suggesting that our system is dominated by viscous forces. The Lenormand phase diagram (Figure 5.18), which was developed from 2D fluid flow through micro-models, is used to explore the role that viscous forces play in experimental outcomes.

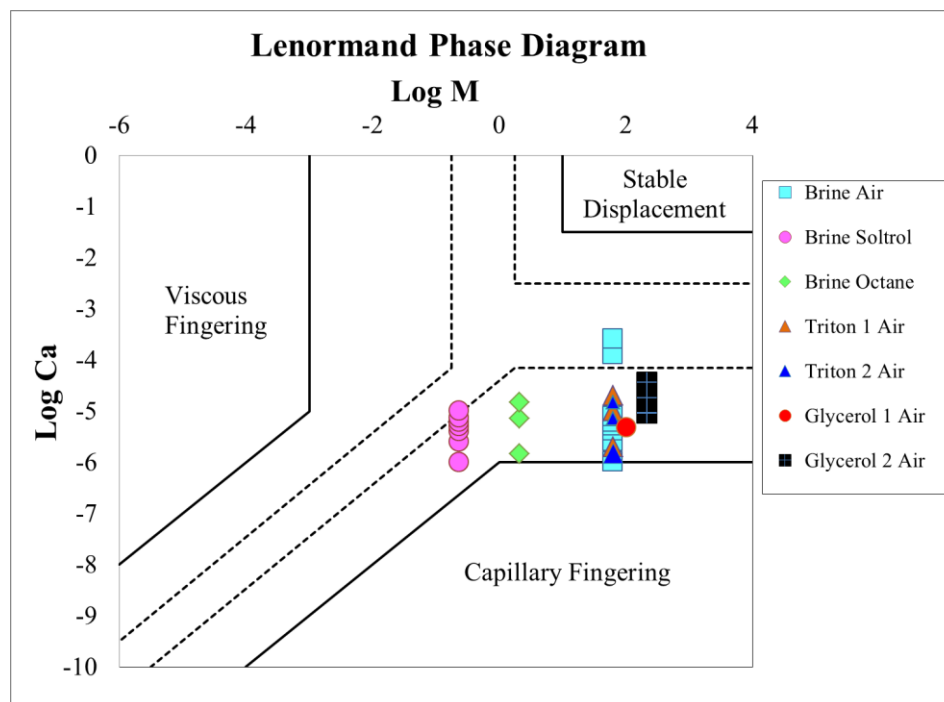


**Figure 5.18: Proxy fluid experimental capillary number and mobility ratios plotted as a Lenormand phase diagram.**

The phase diagram is generally used to establish the three fluid displacement regimes (viscous fingering, capillary fingering, and stable displacement) that dominate flow in the pore space, as originally described by Lenormand et al., (1983). Figure 5.18 shows these regimes, along with the experimental data, on a logarithmic capillary number and mobility ratio scale. It should be noted that these regimes were developed based on 2D flow in porous micro-models and the boundaries of the displacement regimes are subject to change depending on the porous media (Zhang et al., 2011). This would explain why our experiments (shown on Figure 5.18) appear to fall in the capillary fingering zone despite the evidence that viscous, not capillary forces, dominate in our system.

Further proof that viscous forces play a large role in fluid displacement behavior in our system is provided by an evaluation of the capillary-to-gravity ratio (CGR). The product of the capillary number (viscous/capillary forces) and the CGR (capillary/gravitational forces) yields a ratio of viscous to gravitational forces. This product (which is labeled as ‘Ca·CGR’) was plotted against the CGR in Figure 5.19. Since the CGR is dependent on bead size (as permeability is calculated from grain size which is demonstrated by eq. 2.7), the open symbol data points represent the smallest beads (600  $\mu\text{m}$ ) and the closed data points represent the largest beads (1400  $\mu\text{m}$ ).

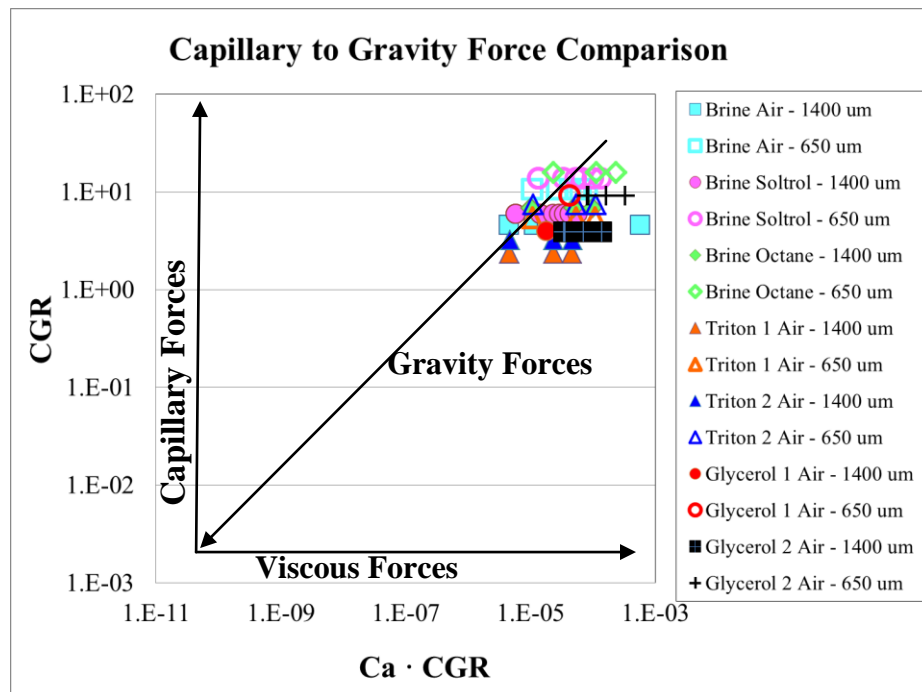


**Figure 5.19:** A plot of the product between capillary number (Ca) and the capillary-to-gravity ratio (CGR) versus the CGR.

All of the data points in Figure 5.19 have Ca·CGR values ranging from  $10^{-6}$  –  $10^{-3}$  and CGR values ranging from orders of magnitude  $10^0$  –  $10^1$ . This plot can be used in conjunction the findings from Polak et al., (2011) which identified the relative dominance of capillary, viscous

and gravitational forces, as designated by the three force arrows on Figure 5.19. According to this figure, our system, with relatively large Ca-CGR ratios, is out of the gravity dominated regime and into a viscous force dominating regime.

Viscous forces (or viscous fingering) have historically been manipulated to enhance the *removal* (or mobilization) of non-wetting phase fluids from formations through miscible fluid flooding events (e.g. enhanced oil recovery) (Juanes and Blunt, 2006). However, based on our results we suggest that engineering a system in which viscous forces dominate (through alterations made to the non-wetting phase viscosity) could also be advantageous for increased residual non-wetting phase trapping applications, specifically geological CO<sub>2</sub> sequestration.

## Chapter 6: Conclusions

The optimization of the capillary trapping mechanism for application in CO<sub>2</sub> sequestration was investigated by proxy fluid pair experiments on an unconsolidated glass bead pack. Alterations were made to fluid flow rate, wetting and non-wetting fluid viscosity, and interfacial tension to determine the relative effectiveness of each of the three parameters on residual non-wetting phase trapping efficiency. These three parameters are often presented in the form of the capillary number, a dimensionless number depicting the balance between viscous and capillary forces.

Capillary number and its effects on initial and residual trapping has been well researched, the common consensus being that trapped non-wetting phase will increase with decreasing capillary number. Our residual saturation data, which was collected from experiments that altered and isolated the individual elements of capillary number, did not increase or decrease with increasing capillary number.

Contrary to recent research (Juanes et al., 2006; Bachu and Bennion, 2008), injection flow rate and interfacial tension did not have an impact on the amount of trapped residual non-wetting phase. We note that values of interfacial tension were only varied by approximately a factor of three, as opposed to flow rate and viscosity values which were each varied by several orders of magnitude. Experiments that vary interfacial tension to a larger degree may provide greater insight into role that interfacial tension plays in capillary trapping.

The non-wetting phase viscosity emerged as the most important element of capillary number as volumes of trapped non-wetting phase increased with increasing non-wetting proxy fluid

viscosity. The largest residual non-wetting saturation was approximately 40%, significantly higher than previously published fluid flow through glass bead pack saturations at capillary numbers ranging from  $10^{-4}$  –  $10^{-3}$  (Morrow et al., 1988; Suekane et al., 2010). Additional experimentation at these higher capillary numbers would be helpful in fully characterizing fluid flow behavior in glass bead columns.

The Lenormand phase diagram is a useful tool for evaluating fluid displacement mechanisms at the pore-scale. However, it was originally developed for a 2D micro-model and displacement regimes have been shown to change depending on the type of porous structure. We would therefore not necessarily expect our Lenormand fluid displacement regime boundaries to be in the same location as the original Lenormand phase diagram. Based on the relationship between residual non-wetting saturation and non-wetting fluid viscosity, we conclude that our experiments likely fall in the viscous fingering regime, instead of the well documented capillary fingering regime. This conclusion is supported by a plot of the mobility ratio and the capillary-to-gravity diagram, both of which indicate that viscous forces dominate in our system.

Immobilized residual non-wetting phase was spatially correlated to original non-wetting phase via the original saturation dependence. The magnitude (slope) of the dependence varied depending on fluid pairs present in the pore space, but a trend of increasing wetting and non-wetting fluid viscosity and decreasing original non-wetting saturation was evident. The broader impact of this finding is that the amount of  $\text{CO}_2$  injected during sequestration will be affected by the amount of non-wetting phase already present in the formation. To optimize the amount of  $\text{CO}_2$  injected during a sequestration project, alterations can be made to enhance the viscosity of the  $\text{CO}_2$ . Supercritical  $\text{CO}_2$  with higher viscosity will be less dependent on any in-situ non-

wetting fluid in the formation and will increase the overall residual trapping efficiency of the project.

## Future Work

Original saturation dependences should be calculated for other types of media (e.g. consolidated media) to observe if and how the behavior (trend lines) of the dependencies changes.

Additional experimentation encompassing a wider range of capillary numbers could be useful in determining the behavior of capillary trapping in glass beads. This may translate to experiments that are conducted at faster flow rates or the creation of solutions with decreased IFT values (an order of magnitude lower than those presented in this work). Ultimately, similar experiments need to be performed using brine and supercritical CO<sub>2</sub> to determine if the same conclusions can be drawn on a system that more closely resembles that of an actual sequestration scenario.

## Bibliography

Aissaoui, A. (1983). Etude théorique et expérimentale de l'hystérésis des pressions capillaires et des perméabilités relatives en vue du stockage souterrain de gaz. Ecole des Mines de Paris. Paris. **PhD**.

Bachu, S. and B. Bennion (2008). "Effects of in-situ conditions on relative permeability characteristics of CO<sub>2</sub>-brine systems." Environmental Geology(54): 1707-1722.

Bachu, S., W. D. Gunter, et al. (1994). "Aquifer Disposal of CO<sub>2</sub>: Hydrodynamic and Mineral Trapping." Energy conversion and management **35**(4): 269-279.

Bandara, U. C., A. M. Tartakovsky, et al. (2011). "Pore-scale Study of capillary trapping mechanism during CO<sub>2</sub> injection in geological formations." International Journal of Greenhouse Gas Control **5**(6): 1566-1577.

Bennion, B., and Bachu, S. (2006a). The Impact of Interfacial Tension and Pore Size Distribution/Capillary Pressure Character on CO<sub>2</sub> Relative Permeability at Reservoir Conditions in CO<sub>2</sub>-Brine Systems. SPE/DOE Symposium on Improved Oil Recovery. Tulsa, Oklahoma, Society of Petroleum Engineers. **SPE 99325**.

Bennion, B. and S. Bachu (2005). Relative Permeability Characteristics for Supercritical CO<sub>2</sub> Displacing Water in a Variety of Potential Sequestration Zones in the Western Canada Sedimentary Basin. SPE Annual Technical Conference and Exhibition Dallas, Texas, Society of Petroleum Engineers.

Bennion, D. B. and S. Bachu (2006b). Dependence on Temperature, Pressure and Salinity of the IFT and Relative Permeability Displacement Characteristics of CO<sub>2</sub> Injected in Deep Saline Aquifers. SPE Annual Technical Conference and Exhibition. San Antonio, Texas, Society of Petroleum Engineers. **SPE 102138**.

Bennion, D. B. and S. Bachu (2006c). Supercritical CO<sub>2</sub> and H<sub>2</sub>S-Brine Drainage and Imbibition Relative Permeability Relationships for Intergranular Sandstone and Carbonate Formations. SPE Europe/EAGE Conference and Exhibition. Vienna, Austria, Society of Petroleum Engineers. **SPE 99326**.

Benson, S.M, et al. (2005). Underground geological storage: IPCC special report on carbon dioxide capture and storage. Cambridge University Press. Cambridge, U.K. Chapter 5.

Blunt, M. J. and H. Scher (1995). "Pore-level modeling of wetting." Physical Review E **52**(6).

Cense, A. W. and S. Berg (2009). The Viscous-Capillary Paradox in 2-Phase Flow in Porous Media. International Symposium of the Society of Core Analysts S. I. E. P. B.V. Noordwijk, The Netherlands: 1-12.

Chatzis, I., M. S. Kuntamukkula, et al. (1988). "Effect of Capillary Number on the Microstructure of Residual Oil in Strongly Water-Wet Sandstones." SPE Reservoir Engineering **3**(3): 902-912.

Chatzis, I. and N. R. Morrow (1984). "Correlation of Capillary Number Relationships for Sandstone." SPE Journal **24**(5): 555-562.

Corey, A. T. (1994). Mechanics of Immiscible Fluids in Porous Media. Highlands Ranch, Colorado, Water Resources Publications.

Ding, M. and A. Kantzas (2007). "Capillary Number Correlations for Gas-Liquid Systems." Journal of Canadian Petroleum Technology **46**(2): 27-32.

DOE and NETL (2007). U.S. Department of Energy (DOE) and National Energy Technology Laboratory (NETL) Carbon Sequestration Technology Roadmap and Program Plan. US DOE and NETL. available at:  
[http://www.netl.doe.gov/technologies/carbon\\_seq/refshelf/project%20portfolio/2007/2007Roadmap.pdf](http://www.netl.doe.gov/technologies/carbon_seq/refshelf/project%20portfolio/2007/2007Roadmap.pdf)

Dullien, F. A. L. (1992). Porous Media Fluid Transport and Pore Structure. San Diego, Academic Press.

Ennis-King, J. and L. Paterson (2005). "Role of Convective Mixing in the Long-Term Storage of Carbon Dioxide in Deep Saline Formations." SPE Journal **10**(3): 349-356.

Gladkikh, M. and S. L. Bryant (2006). "Influence of wettability on petrophysical properties during imbibition in a random dense packing of equal spheres." Journal of Petroleum Science and Engineering **52**: 19-34.

Gunter, W. D., B. Wiwchar, et al. (1997). "Aquifer disposal of CO<sub>2</sub>-rich greenhouse gases: extension of the time scale of experiment for CO<sub>2</sub>-sequestering reactions by geochemical modelling." Mineralogy and Petrology **59**: 121-140.

Heiss, V. I., I. Neuweiler, et al. (2011). "Experimental investigation on front morphology for two-phase flow in heterogeneous porous media." Water Resources Research **47**(W10528): 1-7.

Iglauer, S., A. Paluszny, et al. (2011). "Residual CO<sub>2</sub> imaged with X-ray micro-tomography". *Geophysical Research Letters*. **38**: L21403.

IPCC (2001). *IPCC Third Assessment Report - Climate Change 2001 (Intergovernmental Panel on Climate Change)*. IPCC.

IPCC (2005). *IPCC Special Report on Carbon Dioxide Capture and Storage (Intergovernmental Panel on Climate Change, 2005)*. IPCC. Geneva.

Juanes, R. and M. J. Blunt (2006). "Analytical Solutions to Multiphase First-Contact Miscible Models with Viscous Fingering." *Transport in Porous Media* **64**: 339-373.

Juanes, R., E. J. Spiteri, et al. (2006). "Impact of relative permeability hysteresis on geological CO<sub>2</sub> storage." *Water Resources Research* **42**(W12418): 1-13.

Kantzas, A., M. Ding, et al. (2001). "Residual Gas Saturation Revisited." *SPE Reservoir Evaluation & Engineering* **4**(6): 467-476.

Kumar, A., J.P. Middleton, et al. (2009). "Quantifying Trapped Residual Oil in Reservoir Core Material at the Pore Scale: Exploring the Role of Displacement Rate, Saturation History and Wettability." 2009 International Petroleum Technology Conference held in Doha, Qatar 7-9 Decemeber 2009. IPTC 14001.

Kumar, A., M. Noh, et al. (2004). "Reservoir Simulation of CO<sub>2</sub> Storage in Deep Saline Aquifers." *SPE Journal* **10**(3): 336-348.

Lenormand, R., E. Touboul, et al. (1988). "Numerical models and experiments on immiscible displacements in porous media." *Journal of Fluid Mechanics* **189**: 165-187.

Lenormand, R., C. Zarcone, et al. (1983). "Mechanisms of the displacement of one fluid by another in a network of capillary ducts." *Journal of Fluid Mechanics* **135**: 337-353.

Morrow, N. R., I. Chatzis, et al. (1988). "Entrapment and Mobilization of Residual Oil in Bead Packs." *SPE Reservoir Engineering* **3**(3): 924-934.

Nguyen, V. H., A. P. Sheppard, et al. (2006). "The effect of displacement rate on imbibition relative permeability and residual saturation." *Journal of Petroleum Science and Engineering* **52**: 54-70.

Nordbotten, J. M., M. A. Celia, et al. (2004). "Analytical solutions for leakage rates through abandoned wells." Water Resources Research **40**(W04204).

Pentland, C. H., et al. (2008). "Measurement of Non-Wetting Phase Trapping in Sand Packs." 2008 SPE Annual Technical Conference and Exhibition held in Denver, Colorado USA, 21-24 September 2008. **SPE 115697**.

Pentland, C. H., et al. (2010). "Measurement of Nonwetting-Phase Trapping in Sandpacks." SPE Journal **15**(2): 274-281.

Pentland, C.H., R. El-Maghraby, et al. ( 2011). "Measurements of capillary trapping of supercritical carbon dioxide in Berea sandstone." Geophysical Research Letters **38**: L06401.

Pini, R., S. Krevor, et al. ( 2012). "Capillary pressure and heterogeneity for CO<sub>2</sub>/water system in sandstone rocks at reservoir conditions." Advances in Water Resources **38**: 48-59.

Piri, M. and M. J. Blunt ( 2005). "Three-dimensional mixed-wet random pore-scale network modeling of two- and three-phase flow in porous media. I. Model description." Physical Review E **71**(2): 026301.

Polak, S., Y. Cinar, et al. (2011). "An experimental investigation of the balance between capillary, viscous, and gravitational forces during CO<sub>2</sub> injection into saline aquifers." Energy Procedia **4**: 4395-4402.

Riaz, A., M. Hesse, et al. (2006). "Onset of convection in a gravitationally unstable diffusive boundary layer in porous media." Journal of Fluid Mechanics **548**: 87-111.

Rutqvist, J. and C.-F. Tsang (2002). "A study of caprock hydromechanical changes associated with CO<sub>2</sub>-injection into a brine formation." Environmental Geology **42**: 296-305.

Saeedi, A. and R. Rezaee (2012). "Effect of residual natural gas saturation on multiphase flow behaviour during CO<sub>2</sub> geo-sequestration in depleted natural gas reservoirs." Journal of Petroleum Science and Engineering **82-83**: 17-26.

Schrag, D. P. (2007). "Preparing to capture carbon." Science **315**(5813): 812-813.

Shen, P., B. Zhu, et al. (2010). "An Experimental Study of the Influence of Interfacial Tension on Water-Oil Two-Phase Relative Permeability " Transport in Porous Media **85**: 505-520.

- Silin, D., L. Tomutsa, et al. (2011). "Microtomography and Pore-Scale Modeling of Two-Phase Fluid Distribution." Transport in Porous Media **86**: 495-515.
- Spiteri, E. J., R. Juanes, et al. (2008). "A New Model of Trapping and Relative Permeability Hysteresis for All Wettability Characteristics." SPE Journal **13**(3): 277-288.
- Suekane, T., T. Nobuso, et al. (2008). "Geological storage of carbon dioxide by residual gas and solubility trapping." International Journal of Greenhouse Gas Control **2**: 58-64.
- Suekane, T., N. H. Thanh, et al. (2009). "Direct measurement of trapped gas bubbles by capillarity on the pore scale." Energy Procedia **1**(1): 3189-3196.
- Suekane, T., N. Zhou, et al. (2010). "Direct Observation of Trapped Gas Bubbles by Capillarity in Sandy Porous Media." Transport in Porous Media **82**: 111-122.
- Valvatne, P. H. and M. J. Blunt (2004). "Predictive pore-scale modeling of two-phase flow in mixed wet media." Water Resources Research **40**(W07406).
- WEC (2007). World Energy Council 2007 Survey of Energy Resources. W. E. Council. London.
- Wildenschild, D., J. W. Hopmans, et al. (2002). "Using X-ray computed tomography in hydrology: systems, resolutions, and limitations." Journal of Hydrology **267**: 285-297.
- Xu, T., J. A. Apps, et al. (2004). "Numerical simulation of CO<sub>2</sub> disposal by mineral trapping in deep aquifers." Applied Geochemistry **19**: 917-936.
- Zhang, C., M. Oostrom, et al. (2011). "Influence of Viscous and Capillary Forces on Immiscible Fluid Displacement: Pore-Scale Experimental Study in a Water-Wet Micromodel Demonstrating Viscous and Capillary Fingering." Energy and Fuels **25**: 3493-3505.